Persistent cortical excitatory neuron dysregulation in adult *Chd8* haploinsufficient mice.

Cesar P. Canales*[1,2,3], Stephanie Lozano*[1], Nicholas A. Frost[6], Karol Cichewicz[1, 2], Wellington Amaral[3], Nicolas Seban[1], Ethan Fenton[1], Ayanna Wade[1], Nickolas Chu[1], Emily Smith[1], Cory Ardekani[1], Samuel Frank[3], Jeffrey Bennett[3], Pierre Lavenex[4], Aspen Kopley-Smith[1], Darlene Rahbarian[1], Melissa Corea[1], Daniela Perla[1], Liam Davis[1], Jiyuan Zhu[1], Rebecca Ortiz[1], Paris Beauregard[1,2], Caitlin Moyer[5], Jacob Baker[5], Jingqi Sun[5], Boxuan Ma[5], Ju Lu[5,8], Vikaas S. Sohal[7], David Amaral[1,2,3], Yi Zuo[5], Alex S. Nord[1,2,3]

Affiliations:

1) UC Davis Center for Neuroscience, Davis, CA 95618, USA

2) Department of Psychiatry and Behavioral Sciences, University of California Davis, Sacramento, CA 95817, USA

3) The M.I.N.D. Institute, UC Davis, Sacramento, CA, USA

4) Laboratory of Brain and Cognitive Development, Institute of Psychology, University of Lausanne, Switzerland

5) Department of Molecular, Cell and Developmental Biology, University of California Santa Cruz, Santa Cruz, CA 95064, USA

6) University of Utah, Department of Neurology, Salt Lake City, Utah, United States of America

7) Department of Psychiatry and Behavioral Sciences, University of California, San Francisco | Weill Institute for Neurosciences, University of California, San Francisco | Kavli Institute for Fundamental Neuroscience, University of California, San Francisco

8) Present address: Department of Biological Sciences, Lehigh University, Bethlehem, PA 18015, USA

* These authors contributed equally

Abstract

CHD8 mutations cause autism spectrum disorder, cognitive deficits, and macrocephaly. *Chd8*$^{+/-}$ mouse models exhibit macrocephaly and transcriptional pathology, with inconsistent findings regarding neurogenesis, neuron function, and behavior. Via stereology and single nuclei transcriptomics (snRNA-seq), we found increased *Chd8*$^{+/-}$ cortical volume was not explained by increase in neuron number. Differential expression (DE) was present across cortical cell types, with excitatory neurons exhibiting high DE burden and shared and subclass-specific DE signatures. Bulk RNA-seq DE of constitutive *Chd8*$^{+/-}$ and conditional *Camk2a-Cre Chd8*$^{+/-}$ mice identified shared transcriptional pathology. DE in synaptosomal versus nuclear mRNA identified overlapping DEGs, but also significant differences and exaggerated synaptosomal changes. Building on DE findings implicating glutamatergic neurons, we found *Chd8*$^{+/-}$ mice exhibited altered excitatory neuron spine density and dynamics, decreased GCaMP activity correlation, and sleep perturbation. Thus, *Chd8* haploinsufficiency causes lasting excitatory neuron dysfunction, perturbs RNA regulation beyond transcription, and impacts neuronal properties, cortical microcircuits, and behavior.

42 **Introduction**

43 Mutations in a growing list of genes cause monogenic Neurodevelopmental Disorders (NDDs) with
44 overlapping but complex presentation, including autism spectrum disorder (ASD), intellectual disability
45 (ID), and behavior or psychiatric disorders[1,2]. *CHD8* encodes the chromatin remodeling factor (CRF)
46 Chromodomain Helicase DNA-binding protein 8, and has among the highest rates of protein disrupting
47 rare and de novo mutations in ASD cases[1]. CHD8-associated NDD (*CHD8*-NDD) has core but variably
48 expressed features including ASD, ID, and macrocephaly, as well as sleep, gastrointestinal, psychiatric,
49 and neurological issues[3–9]. *CHD8* is ubiquitously expressed and has pleiotropic functions in the
50 developing and mature brain. Clarifying the links between *CHD8* haploinsufficiency, macrocephaly, and
51 pathology may offer critical insights into the etiology of the 15% of ASD patients that exhibit more
52 severe cognitive and behavioral phenotypes often with poorer prognosis[10]. Furthermore, Chd8 has
53 been identified as a central regulator in network studies of ASD-associated loci[11–13], and serves as a
54 key example of the many CRF genes implicated in ASD and other NDDs[14–18]. Defining the pathological
55 consequences associated with *CHD8* haploinsufficiency is thus an important step towards
56 understanding both *CHD8*-specific mechanisms and broader NDD neurobiology.

57 *Chd8* knockout is embryonic lethal in mice[19,20], and NDD-relevant phenotypes have been observed
58 across studies of heterozygous *Chd8*$^{+/-}$ mouse models[20–26]. Among the consistent findings across
59 constitutive *Chd8*$^{+/-}$ mouse models is the presence of adult macrocephaly and transcriptional
60 pathology[20,22,24,25]. Bulk RNA-seq on developing and adult *Chd8*$^{+/-}$ mouse brain has been performed in a
61 number of studies, finding relatively subtle effects but replicated perturbation of energetics and protein
62 homeostasis and downregulation of synaptic and neuronal genes[20,21,24,25,27–30]. Recent single cell
63 studies of *Chd8*$^{+/-}$ mice suggest subtle changes in neurodevelopment and perturbations to neurons[31–33],
64 but have lacked resolution to analyze specific subtypes in mature cortex. Studies of *Chd8*$^{+/-}$ mouse
65 behavior and cognition have been more variable[20–26], with evidence that some variability is due to
66 genetic background[34,35]. Multiple studies of Chd8 haploinsufficiency have identified changes to
67 electrophysiology in the cortex and in in vitro[21,24,36,37], indicating impacts on neuron function. In vitro

68 studies in human and non-human primate neurons and human cortical organoids also indicate
69 perturbation to neurogenesis, increases in organoid size paralleling macrocephaly, and neuronal
70 electrophysiological and network level dysfunction[31,32,38–41]. Finally, conditional *Chd8* knockout studies
71 have been conducted targeting specific cell types such as excitatory neurons[36,42–46], oligodendrocytes[47–
72 49], and astrocytes and microglia[50,51]. Many of these studies have primarily focused on homozygous
73 conditional mutants, which may not accurately model the heterozygous mutations relevant to NDDs.

74 Despite extensive study of *Chd8* as a representative NDD risk gene, key questions remain regarding
75 how heterozygous mutation leads to pathology at the cellular, molecular, and circuit level. First, no
76 published studies have linked adult macrocephaly to changes in cellular composition or described cell-
77 type specific molecular pathology in adult *Chd8*$^{+/-}$ mouse brain. Second, it remains unclear whether
78 neuronal dysfunction has arisen from developmental disruption or reflects a continued requirement for
79 full *Chd8* dosage in mature neurons, and whether reported RNA expression changes are due to
80 transcriptional or post-transcriptional mechanisms. Third, circuit-level consequences to behavior
81 beyond sociability and cognition remain largely unexplored. To address these gaps, we characterized
82 adult *Chd8*$^{+/-}$ mice and cerebral cortex across cellular, molecular, functional, and behavioral domains
83 (**Figure 1A**). Our findings reveal selective vulnerability of cortical glutamatergic neurons to *Chd8*
84 haploinsufficiency, implicate disrupted post-transcriptional regulation of synaptosomal RNA
85 homeostasis, and demonstrate associated changes in dendritic spine dynamics, impaired neuronal
86 signaling coherence, and altered sleep architecture in *Chd8*$^{+/-}$ mice.

87 **Results**

88 <u>*Description of Chd8 mutant mouse lines*</u>

89 Constitutive mutant *Chd8* mice were generated on the C57BL/6N background via CRISPR/Cas9
90 targeting exon 5, resulting in a 5 bp deletion that leads to reduced *Chd8* mRNA and protein and is early
91 embryonic homozygous lethal. We previously characterized heterozygous mutants from this line
92 (referred to as *Chd8*$^{+/5bpdel}$, herein *Chd8*$^{+/-}$), reporting differential expression and splicing, altered cortical

93 proliferation, increased brain volume, and phenotypes of altered exploration in open field assay and
94 deficits in fear conditioning and novel object recognition[20]. We also use a conditional *Chd8* loxP mutant
95 on the C57BL/6J background generated by Jackson Laboratory where exon 3 is ablated in the
96 presence of CRE (*Chd8*^{em3Lutzy}). These were mated to *Camk2a*-CRE (B6.Cg-Tg(Camk2a-cre)T29-
97 1Stl/J; JAX strain: 005359) to direct conditional heterozygous ablation in post-mitotic forebrain
98 glutamatergic neurons in this line, herein referred to as *Chd8*$^{+/flox}$.

99 *Increased adult cortical volume without increase in neuron number or soma size in Chd8*$^{+/-}$ *mice*

100 We previously identified increased cortical volume and macrocephaly in *Chd8*$^{+/-}$ mice via structural
101 MRI[20]. Here, we aimed to replicate this finding and determine whether the volume increase results from
102 a higher number of neurons. We performed unbiased stereological analysis on Nissl-stained brain
103 sections from male and female heterozygous *Chd8*$^{+/-}$ mice and wild-type littermates at postnatal day 42
104 (P42) (**Figure 1B-C**), an age marking the end of adolescence and a mature stage of mouse brain
105 development[52]. We examined 15–18 representative coronal sections per mouse using established
106 stereological methods to accurately assess cortical volume, neuronal distribution, and soma size.
107 Cortical volume was estimated using the Cavalieri method[53,53,54], revealing a significant overall increase
108 in *Chd8*$^{+/-}$ mice compared to wild-type littermates (**Figure 1D**, P=0.032, Student's t-test). When
109 stratified by sex, the increase in cortical volume was more pronounced and independently significant in
110 males (P=0.009 males; P=0.61 females, Student's t-test) (**Supplement**). Comparing volume across
111 rostral-caudal sections, *Chd8*$^{+/-}$ males showed increase in more rostral regions (**Supplement**).

112 Next, we investigated whether the cortical volume expansion was associated with an increase in
113 neuronal numbers or soma size. Using the optical fractionator method[55], we estimated neuron counts
114 across the cortex. We did not find significant differences in total neuron number in either the full cohort
115 or sex-stratified analyses (P=0.76, unstratified; P=0.37, males; P=0.3, females) (**Figure 1E**). Finally, we
116 assessed neuronal soma size and found no significant differences between genotype groups in full or
117 sex-stratified analyses (P=0.23, unstratified; P=0.81, males; P=0.19, females) (**Supplement**). Taken

together, these findings replicate the cortical volume increase observed in *Chd8*$^{+/-}$ mice, with a stronger effect in males, and demonstrate that this expansion is not explained by an increase in neuronal number or soma size. Instead, the increased cortical volume without an increase in numbers results in decreased glutamatergic neuron density in the *Chd8*$^{+/-}$ cortex.

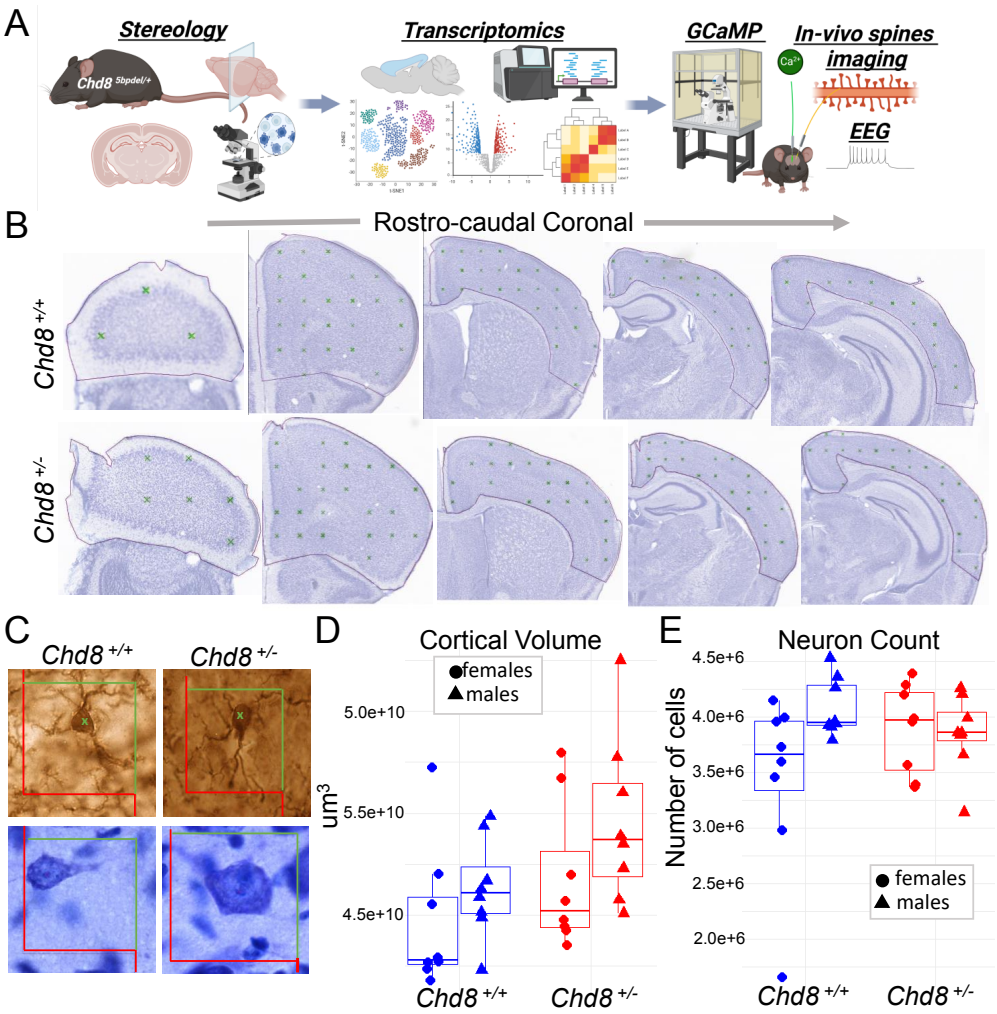

Figure 1. Increased cortical volume in *Chd8*$^{+/-}$ mice without a corresponding increase in neuron number. (A) Schematic overview of study investigating the role of *Chd8* haploinsufficiency in mature mouse cortex. (B–C) Representative coronal sections across the rostro-caudal extent of the cerebral cortex used for unbiased stereological analysis. (B) Cortical boundaries as determined for volume measurements. (C) Cellular organization visualized using Nissl staining (top) and NeuN immunostaining (bottom) in *Chd8*$^{+/+}$ and *Chd8*$^{+/-}$ mice. (D–E) Stereological profiles across the Z-plane showing (D) cortical volume estimates based on the Cavalieri method and (E) total neuron number as assessed by unbiased stereology in the same rostro-caudal regions. Data are stratified by sex and genotype. Error bars represent SEM. Statistical comparisons were performed using two-way ANOVA (Cortical volume: P=0.032 unstratified, P=0.009 males; P=0.61 females; Neuron Count: P=0.76, unstratified; P=0.37, males; P=0.30, females Student's t-test need to insert n per group).

134 *Cell-type specific cellular and molecular pathology in Chd8$^{+/-l}$ P60 cortex*

135 Towards characterizing differences in RNA expression associated with *Chd8* haploinsufficiency in adult
136 (P60) mouse cortex, we performed single nucleus RNA sequencing (snRNA-seq) on constitutive
137 *Chd8$^{+/-}$* mice, as well as bulk RNA-seq on *Chd8$^{+/-}$* and conditional *Camk2a-CRE Chd8$^{+/flox}$* mutants, and
138 for nuclear and synaptosomal RNA from *Chd8$^{+/-}$* mutants (**Figure 2A**). For snRNA-seq, we analyzed
139 *Chd8$^{+/-}$* (male n = 3, female n= 2) and WT littermates (male n=2, female n=3 WT). Following quality
140 control and ambient RNA correction[56], there were 11,751 and 12,169 nuclei from *Chd8$^{+/-}$* and WT
141 samples, respectively, which we mapped to 18 cortical cell types based on marker gene expression
142 and integration with the BICCN mouse brain atlas[57] (see methods) (**Figure 2B** and **Supplement**).
143 There was balanced representation of male and female samples and of *Chd8$^{+/-}$* and WT samples
144 (**Figure 2C**). *Chd8* expression was higher in non-neuronal cells, but detectable across all cell types
145 (**Figure 2C**). There were no significant differences in *Chd8* expression between mutant and WT cells,
146 as expected based on a cytosolic nonsense-mediated decay being required for reduced levels of the
147 mutant frameshift transcript. All major cortical cell types were identified, with expected expression of
148 marker genes (**Figure 2C**). Cell identity was split at three levels: cell type 3 representing general
149 classes (e.g. glutamatergic neurons), cell type 2 associated with specific canonical subtypes (e.g. L4/5
150 IT), and cell type 1 representing data-driven further sub-clustering of subtypes (e.g. L4/5 IT Glut1).
151 Following UMAP generation and cell type identification, we tested for differences in the relative
152 representation across different cell types, comparing normalized cell proportions between *Chd8$^{+/-}$* and
153 WT groups (**Figure 2E**). At the cell type 2 level, there was significant increase in OPC and decrease in
154 L6 IT, with trending increase in astrocytes and decrease in microglia. These findings are consistent with
155 the results from stereology, demonstrating that macrocephaly and increased cortical volume in *Chd8$^{+/-}$*
156 mice is not due to increase in number of glutamatergic neurons and further suggesting that increased
157 cortical volume is not explained by expansion of specific cell types.

158 Next, we performed cell-type specific differential expression (DE) analysis using a cluster-level
159 pseudobulk framework[58], where reads are from the relevant cell type are aggregated at the sample

level, followed by DE testing using DESeq2[59] with experimental batch included as a covariate. We performed DE analysis at each level of cell type identity, with a focus on cell type 2 for results here. DE results were stablished using either the full dataset or when down-sampling for equivalent cell/nuclei numbers across cell types and when using both uncorrected and ambient RNA corrected expression values, and similar effects were present when stratifying male and female samples (**Supplement**). Comparing DE burden (defined as the number of total DE genes divided by genes passing criteria for

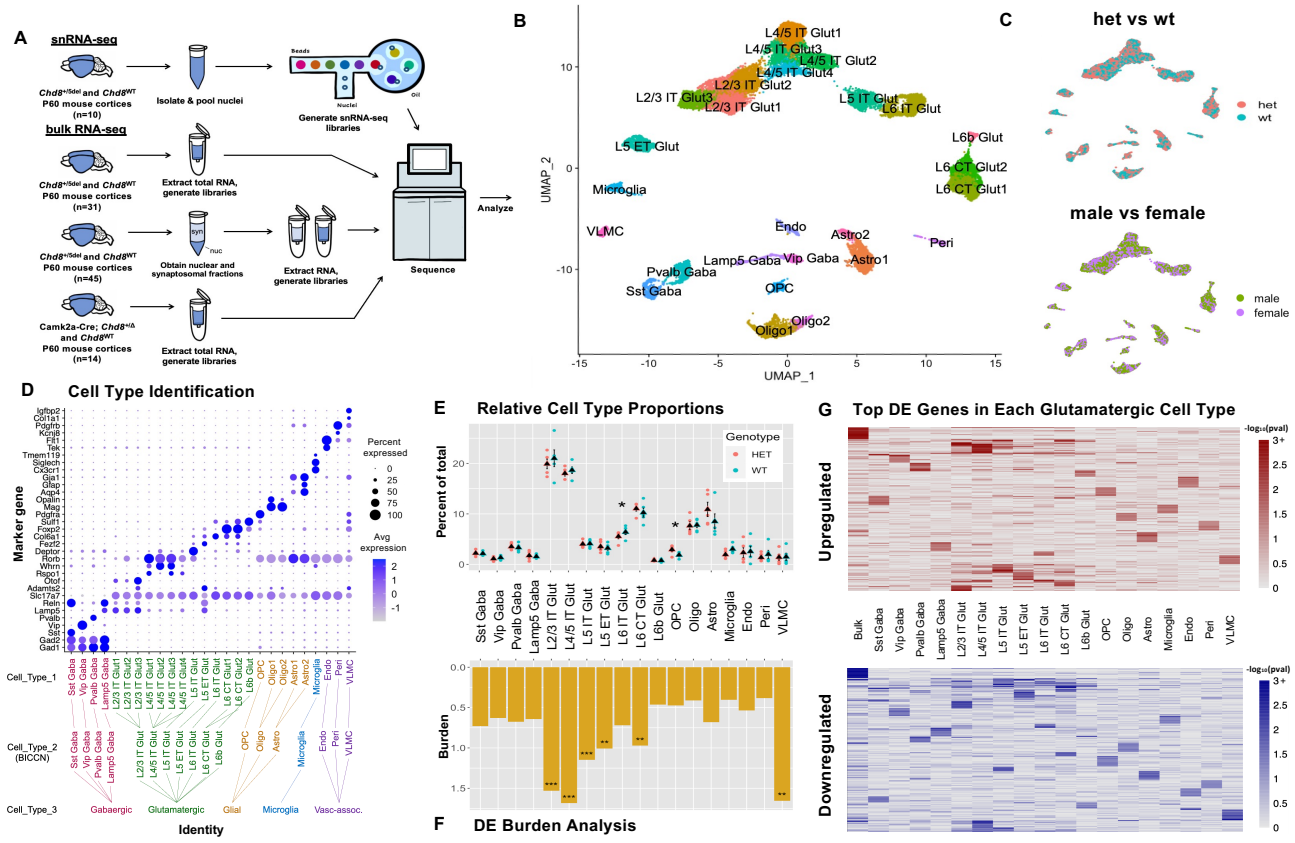

Figure 2: Cell type-specific pathology in adult *Chd8*$^{+/-}$ mouse cortex. A) Schematic depicting experimental design for RNA-seq and snRNA-seq experiments. B) UMAP of 23,920 cortical nuclei from P60 *Chd8*$^{+/-}$ and WT littermates with cell types annotated. C) Clustering of *Chd8*$^{+/-}$ (HET) and WT nuclei (top) and male and female nuclei (bottom) in UMAP space. D) Cell type identification dot plot representing average expression of cell type-specific marker genes in each cell type. Tree (bottom) shows 3 levels of cell type identification (Cell_Type_1-3). E) Cell type proportion comparison between *Chd8*$^{+/-}$ (HET) and WT nuclei, revealing a significant decrease in mutant L6 IT Glut nuclei (*p = 0.027) and increase in mutant OPCs (*p = 0.048) (Student's t-test). F) DEG burden across cell types (Burden = DE genes / expressed genes * 100). Significant DE burden was found in L2/3 IT (*p = 0.00001), L4/5 IT (*p = 0.00001), L5 IT (*p = 0.00001), L5 ET (*p = 0.0045), L6 CT Glut (*p = 0.0004), and VLMC (*p = 0.0009) nuclei (permutation test, n= 10,000). G) Heatmap showing –log10(pval) of top 25 unique upregulated (top) and downregulated (bottom) bulk and pseudobulk DEGs in each cell type (p < 0.1).

179 testing), glutamatergic cell types along with VLMC showed the largest impacts (**Figure 3F**). Among
180 glutamatergic neurons, L2/3 intra-telencephalic (IT) and L4/5 IT neurons had the highest burden. At the
181 single gene level, the top DE genes (DEGs) varied by cell type, with the exception that glutamatergic
182 neuron subtypes, showed considerable overlap in effects (**Figure 3G**). We performed gene set
183 enrichment analysis (GSEA) based on DE rank using the clusterProfiler package[60] (**Supplement**). Only
184 glutamatergic neuron subtypes had DE signatures strongly associated with GO terms (FDR < 0.05),
185 with the strongest signatures in L2/3 IT and L4/5 IT. Using a relaxed threshold of uncorrected P < 0.05,
186 upregulated genes in glutamatergic neurons showed shared enrichment for pathways including
187 *Synapse organization*, *Synaptic signaling*, and *Axon guidance*, and *Neuron differentiation*. Finally, we
188 applied NeuronChat[61] to infer cell-cell communication networks comparing receptor-ligand relationships
189 in *Chd8*$^{+/-}$ and WT cortex based on snRNA-seq data (**Supplement**). This analysis revealed significantly
190 reduced Neurexin-Neuroligan interaction strength and frequency in *Cdh8*$^{+/-}$ mice, with the strongest
191 effect in L2/3 IT neurons (**Supplement**). Conversely, we detected increased communication strength
192 involving glutamate receptors in the *Chd8*$^{+/-}$ mutants (**Supplement**). These findings highlight disrupted
193 synaptic signaling in *Chd8*$^{+/-}$ mice and suggest that glutamatergic neuron subtypes, particularly L2/3 IT
194 and L4/5 IT neurons, are disproportionately affected in the adult cortex.

195 *Shared and cell-type specific DE co-expression modules in Chd8*$^{+/-}$ *glutamatergic neurons*

196 To capture systems-level expression patterns in glutamatergic neurons, we used hdWGCNA[62] to
197 identify gene co-expression modules and then identified differentially expressed modules (DEMs)
198 based on log2-transformed Fold Change (logFC) of module genes (see methods for details). All
199 glutamatergic cell subtypes were used as input to hdWGCNA, which yielded 10 modules accounting for
200 1,691 (17%) genes, with the remaining 8,115 genes assigned to the grey group (**Figure 3A**). 8/10
201 modules were DEMs in at least one glutamatergic subtype, as indicated by highlighted label and box
202 outlines in **Figures 2B-E.** Two modules (M1 and M7) were DEMs across most glutamatergic subtypes,
203 whereas the other six DEMs (M2, M3, M4, M6, M9, and M10) showed genotype differences in only one
204 or two subtypes. Module level differential expression direction and effect size varied, though all but one

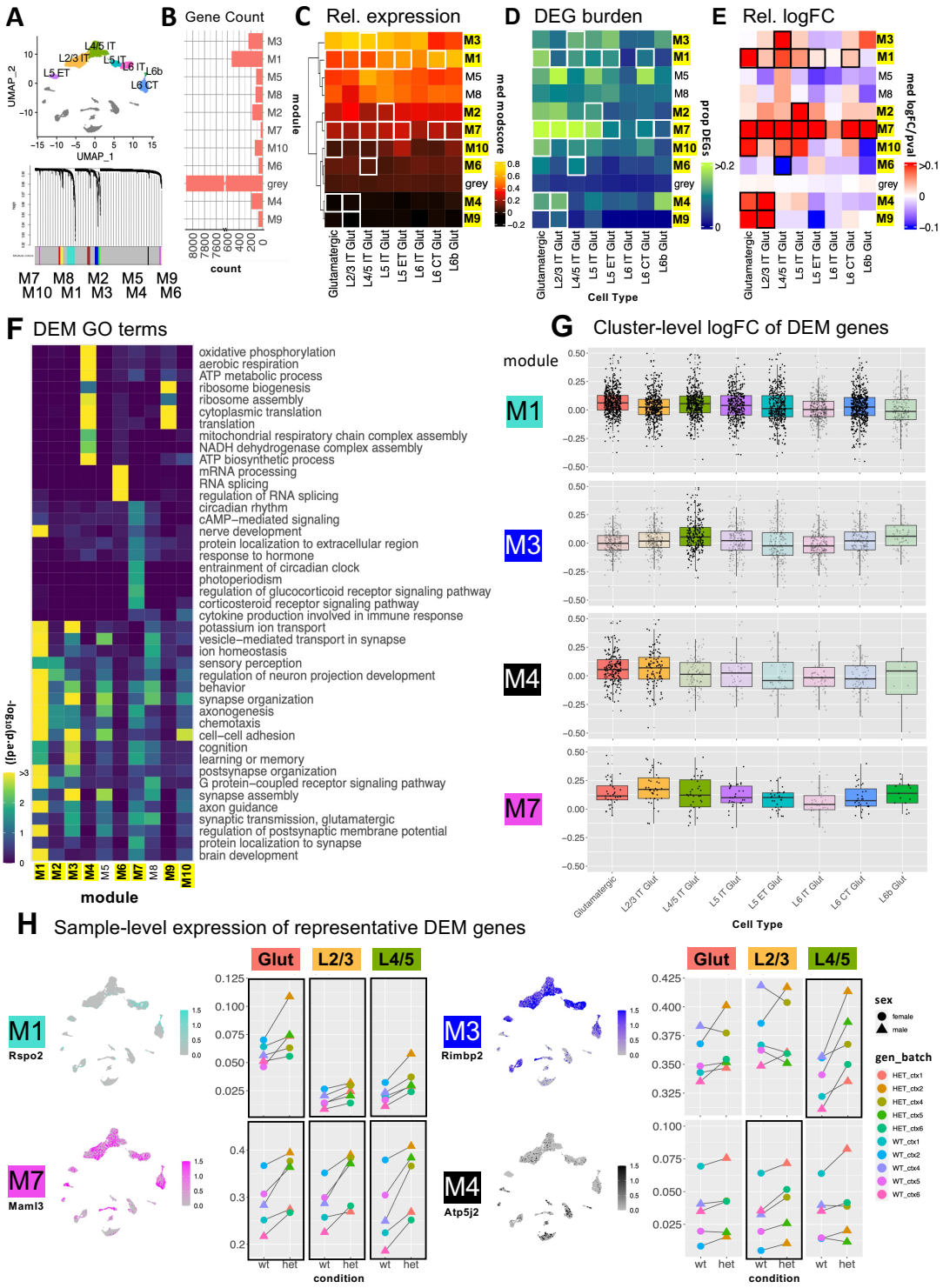

Figure 3: hdWGCNA reveals differentially expressed glutamatergic cell coexpression modules. A) 10 glutamatergic modules identified via hdWGCNA B) Number of genes per module. C) Relative expression of glutamatergic modules across glutamatergic neuron subtypes (module score = average expression of all module genes compared to expression-matched background genes; DEMs identified via comparison of median pseudo-bulk logFC of module genes to that of the grey module via t-test; DEMs (*p < 0.05) in at least one population are labeled in yellow. D) DEG burden (calculated as in Fig. 2F) of each DEM in each cell type E) Heatmap of relative median pseudo-bulk logFC of module genes for glutamatergic cell types scaled by p-value. White and black boxes in C-E indicate the cell types in which each corresponding module was DE. F) Representative significant GO terms for Biological

Processes enriched in glutamatergic modules. (*p < 0.05, **p < 0.01, ***p < 0.001). G) Box plots for 4 representative DEMs showing logFCs of module genes in each glutamatergic subtype. Opaque boxes indicate cell types where the module shown was significantly differentially expressed. H) Feature plots (left) showing relative expression of representative genes from DEMs of interest in UMAP space. Dot plots (right) show median sample-level expression of the same genes. Black boxes indicate cell types where the corresponding module is differentially expressed, or where the direction of change in module expression is consistent across batches.

DEM (M6 in L4/5 IT) were upregulated in *Chd8*$^{+/-}$ mutants. The modules varied in gene number (**Figure 3B**) and relative expression patterns (**Figure 3C**) across glutamatergic subtypes and cortical layers. The proportion of module genes that were individually DE (**Figure 2D**) and the module-level logFC (**Figure 2E**) similarly varied across modules and subtypes.

The glutamatergic co-expression modules showed different association to biological processes based on GO enrichment (**Figure 3F**). First, 6/10 modules showed overlapping enrichment for a variety of general neuron-associated terms (e.g. *Synapse assembly*, *Axon Guidance*, *Behavior*) without strong module-specific GO terms. These included DEMs M1, M2, and M3, as well as non-DEMs M8 and M5. These modules also showed relative expression differences across glutamatergic subtypes and cortical layers, suggesting that co-expression for these gene sets is primarily driven by expression co-variation associated with cell identity, rather than driven by co-expression associated with biological processes or genotype effects. The remaining four modules (M4, M6, M7, M9) were all DEMs and featured strong module-specific GO enrichment: M4 and M9, associated with *Aerobic Respiration* and *Translation* and upregulated in L2/3 IT, M6, associated with *mRNA processing* and downregulated in L4/5 IT, and M7, which was broadly downregulated and associated with general neuronal terms as well as GO terms represented by *Circadian rhythm*. In addition to module-specific GO terms, these four modules did not show subtype- or laminar-associated differences in relative expression and had DE signatures limited to individual glutamatergic subtypes. We highlight gene-level differential expression patterns for DEMs of high interest in **Figure 3G**, focusing on M1 and M7 modules that are broadly DE across glutamatergic subtypes, and M3 and M4 modules that are subtype-specific DEMs with prominent effects in L4/5 IT and L2/3 IT, respectively. **Figure 3H** shows representative gene expression patterns from these DEMs visualized in UMAPs and pseudobulk-level relative expression plots. See

244 **Supplement** for extended modules visualizations. M1 (featuring *Rspo2*) includes a large set of genes
245 that are expressed most highly in deep layer excitatory neurons (L6 CT and L6b), associated with
246 general neuronal and synaptic functions. Although it includes both up- and downregulated genes, M1
247 shows a significant bias towards upregulation with the strongest effects in L4/5 IT and L5 IT subtypes.
248 In contrast, M7 (featuring *Malm3*) is a smaller module exhibiting consistent upregulation across all
249 glutamatergic subtypes. It is associated with general neuronal function as well as circadian rhythm and
250 hormone response pathways. M3 (featuring *Rimbp2*) is selectively upregulated in more superficial
251 glutamatergic subtypes L4/5 IT neurons, with enrichment for neuronal and synaptic processes. In
252 contrast M4 (featuring *Atp5j2*) shows low expression across glutamatergic subtypes and GABAergic
253 neurons, but relatively higher expression in non-neuronal cell types, with gene ontology terms related to
254 translation and mitochondrial ATP metabolism. The shared dysregulation of M1 and M7 DEMs mirrors
255 overlapping GO enrichment patterns across glutamatergic subtypes observed in GSEA (**Supplement**),
256 reflecting convergent molecular pathology. The subtype-specific dysregulation of M3 and M4 suggest
257 genotype-dependent perturbations of distinct biological processes particularly affecting L2/3 IT and L4/5
258 IT neuron populations.

259 *Bulk RNA-seq comparison identifies shared signatures in constitutive versus conditional Chd8 mutants*
260 *but divergent effects in nuclear versus synaptosomal mRNA fractions*

261 We employed bulk RNA-seq as a complementary approach to snRNA-seq, assaying DE signatures
262 across four contrasts: mRNA from P60 cortex from constitutive *Chd8*$^{+/-}$ and from conditional *Camk2a-*
263 *Cre* x *Chd8*$^{+/flox}$ mice, and compartment-enriched nuclear and synaptosomal mRNA from P60 cortex
264 from *Chd8*$^{+/-}$ mice (**Figure 4**). For all conditions, 4-8 biological replicates for each of male and female
265 mutant *Chd8* mice were compared to matched WT littermates, with the primary DESeq2 DE model
266 including sequencing batch and sex as covariates. We also analyzed male and female samples
267 separately, finding generally shared DE signatures (similar as for snRNA-seq) (**Supplement**). Across
268 the four conditions, the largest number of DEGs at either FDR < 0.05 or P < 0.05 was in the
269 synaptosomal preparation, followed by the nuclear preparation, then full cortex from *Chd8*$^{+/-}$ and lastly

270 *Chd8*$^{+/flox}$ (**Figure 4A**). *Chd8* was among the top downregulated DEGs in all but the nuclear mRNA
271 condition, consistent with nonsense-mediated decay of mutant *Chd8* transcripts outside the nucleus
272 (**Figure 4B**). To identify shared and divergent DE signatures across conditions, we compared logFC of
273 DEGs; shared signatures are represented by concordant LogFC direction, condition-specific effects are
274 captured by patterns of change (up or down) in one condition with LogFC around zero in the other
275 condition, and divergent DE signatures are represented by opposite logFC direction. Comparison
276 between *Chd8*$^{+/-}$ and *Chd8*$^{+/flox}$ logFC for genes with FDR < 0.2 and P-value < 0.05 in *Chd8*$^{+/-}$ (**Figure**
277 **4C, Supplement**) captured largely shared signatures, indicating that effects from post-mitotic
278 heterozygous ablation in excitatory neurons accounts for a significant part of DEG transcriptional
279 pathology, DEGs identified in both the nuclear and synaptosomal conditions (FDR < 0.1) showed
280 strong concordance with bulk cortex, however there were striking differences and low concordance
281 between nuclear and synaptosomal enriched mRNA fractions (**Figure 4D**).

282 To compare pathway-level dysregulation across bulk RNA conditions, we used GSEA to identify Gene
283 Ontology (GO) terms where the annotated gene set exhibited significant shift in LogFC distribution
284 towards up- or downregulation, with shared and condition-specific enrichment for representative terms
285 shown in **Figure 4E**. Most of the up- and down-regulated terms identified in the constitutive *Chd8*$^{+/-}$
286 were shared in the conditional *Chd8*$^{+/flox}$, and most terms in the nuclear or synaptosomal enriched
287 conditions were shared in the full cortex preparation, findings that consistent with DEG concordance
288 across contrasts above. We identified shared upregulation of terms including *Cell cycle checkpoint*,
289 *Electron transport chain*, *Mitochondrial translation*, and *Chaperone mediated protein folding*, showing
290 overlap with terms that were also detected in glutamatergic neuron subtypes in the snRNA-seq data
291 (**Supplement** and **Figure 3**). Among upregulated terms that differed between synaptosomal and
292 nuclear conditions were *Regulation of gamma-aminobutyric acid secretion* and *Neuropeptide signaling*
293 *pathway* in the synaptosomal and *Regulation of DNA repair* and *Transport along microtubule* in the
294 nuclear fraction. For downregulated terms, *Axonogenesis*, *Synapse organization*, *Cell adhesion*, and
295 *Regulation of transcription by RNA Pol II* were shared, while *Dendrite morphogenesis* and *Postsynapse*

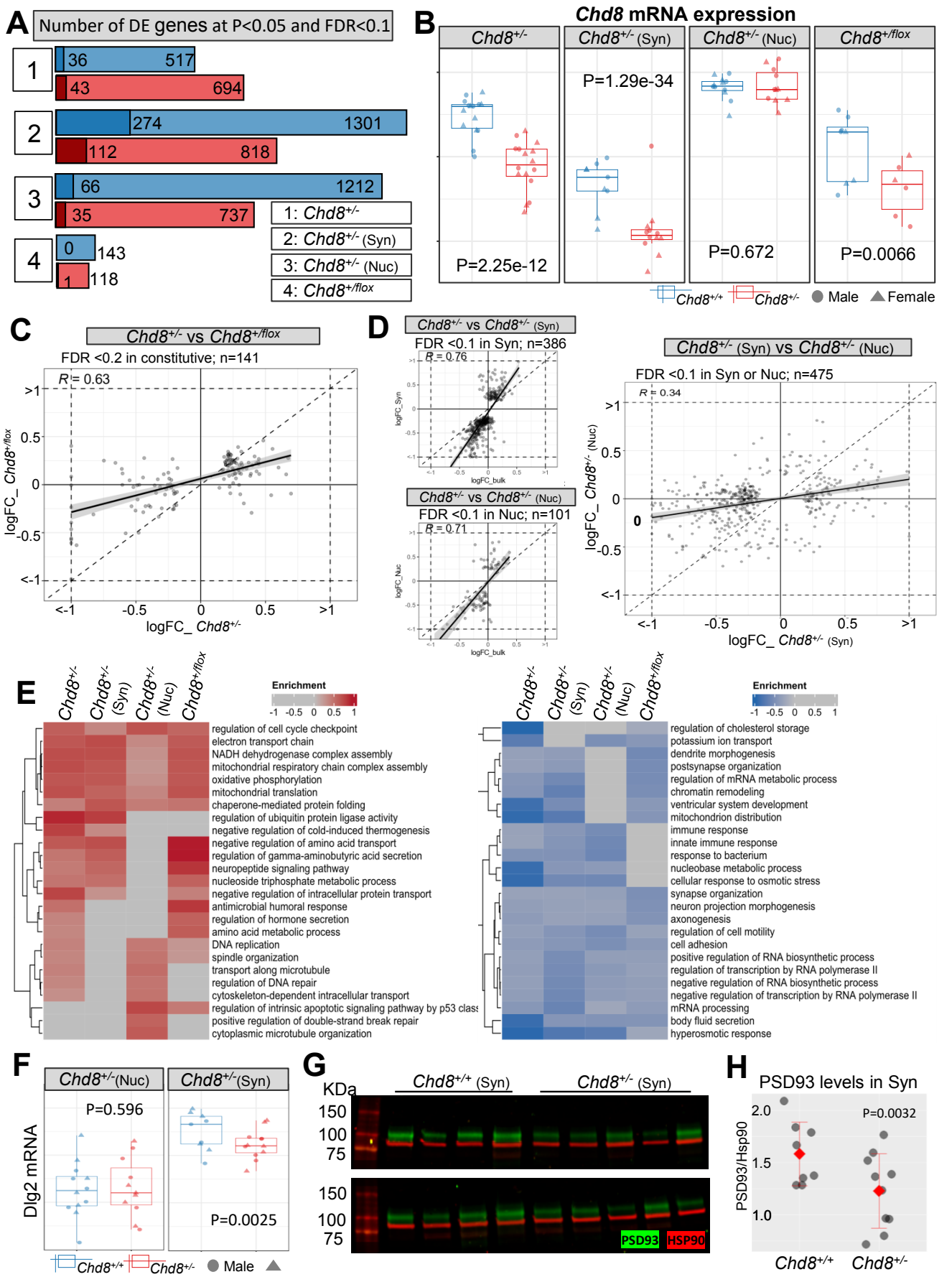
A
Number of DE genes at P<0.05 and FDR<0.1
1
36
517
43
694
2
274
1301
112
818
3
66
1212
35
737
4
0
143
1
118
1: Chd8+/-
2: Chd8+/- (Syn)
3: Chd8+/- (Nuc)
4: Chd8+/flox
B
Chd8 mRNA expression
Chd8+/-
Chd8+/- (Syn)
Chd8+/- (Nuc)
Chd8+/flox
P=1.29e-34
P=2.25e-12
P=0.672
P=0.0066
Chd8+/+
Chd8+/-
Male
Female
C
Chd8+/- vs Chd8+/flox
FDR <0.2 in constitutive; n=141
R = 0.63
logFC_ Chd8+/flox
logFC_ Chd8+/-
D
Chd8+/- vs Chd8+/- (Syn)
FDR <0.1 in Syn; n=386
R = 0.76
logFC_Syn
logFC_bulk
Chd8+/- vs Chd8+/- (Nuc)
FDR <0.1 in Nuc; n=101
R = 0.71
logFC_Nuc
logFC_bulk
Chd8+/- (Syn) vs Chd8+/- (Nuc)
FDR <0.1 in Syn or Nuc; n=475
R = 0.34
logFC_ Chd8+/- (Nuc)
logFC_ Chd8+/- (Syn)
E
Chd8+/-
Chd8+/- (Syn)
Chd8+/- (Nuc)
Chd8+/flox
Enrichment
regulation of cell cycle checkpoint
electron transport chain
NADH dehydrogenase complex assembly
mitochondrial respiratory chain complex assembly
oxidative phosphorylation
mitochondrial translation
chaperone-mediated protein folding
regulation of ubiquitin protein ligase activity
negative regulation of cold-induced thermogenesis
negative regulation of amino acid transport
regulation of gamma-aminobutyric acid secretion
neuropeptide signaling pathway
nucleoside triphosphate metabolic process
negative regulation of intracellular protein transport
antimicrobial humoral response
regulation of hormone secretion
amino acid metabolic process
DNA replication
spindle organization
transport along microtubule
regulation of DNA repair
cytoskeleton-dependent intracellular transport
regulation of intrinsic apoptotic signaling pathway by p53 class
positive regulation of double-strand break repair
cytoplasmic microtubule organization
regulation of cholesterol storage
potassium ion transport
dendrite morphogenesis
postsynapse organization
regulation of mRNA metabolic process
chromatin remodeling
ventricular system development
mitochondrion distribution
immune response
innate immune response
response to bacterium
nucleobase metabolic process
cellular response to osmotic stress
synapse organization
neuron projection morphogenesis
axonogenesis
regulation of cell motility
cell adhesion
positive regulation of RNA biosynthetic process
regulation of transcription by RNA polymerase II
negative regulation of RNA biosynthetic process
negative regulation of transcription by RNA polymerase II
mRNA processing
body fluid secretion
hyperosmotic response
F
Chd8+/-(Nuc)
Chd8+/-(Syn)
P=0.596
P=0.0025
Dlg2 mRNA
Chd8+/+
Chd8+/-
Male
G
KDa
Chd8+/+ (Syn)
Chd8+/- (Syn)
150
100
75
PSD93
HSP90
H
PSD93 levels in Syn
P=0.0032
PSD93/Hsp90
Chd8+/+
Chd8+/-

296

Figure 4: Shared DE in constitutive *Chd8*$^{+/-}$ and *Camk2a-CRE* conditional Chd8$^{+/flox}$ mice, with divergent impacts on nuclear and synaptosomal mRNA and protein. A) Barplot of DEG counts across bulk RNA-seq experiments (constitutive *Chd8*$^{+/-}$, *Camk2a-CRE* conditional *Chd8*$^{+/flox}$, and nuclear and synaptosomal preparations from the *Chd8*$^{+/-}$ line. B) Chd8 is down-regulated in all but the nuclear preparation. C) LogFC concordance between constitutive and conditional datasets for constitutive model DEGs. D) LogFC concordance plots for nuclear and synaptosomal versus whole cortex for DEGs identified in nulear or synaptosomal fractions on left, reduced concordance between nuclear and synapsomal DEG logFC on right. E) Selected enriched GO terms for upregulated (left) and downregulated (right) genes across experiments. F) Downregulation of Dlg2 in synaptosomal RNA. GH) Western blot validating decreased synaptosomal PSD93 protein in *Chd8*$^{+/-}$ cortex.

organization were example synaptosomal-enriched terms. Overall, bulk RNA-seq results from the full cortex and from the nuclear and synaptosomal conditions showed evidence of concordance with DEG findings from snRNA-seq, though with fairly substantial overall differences in DE signatures (**Supplement**). The nuclear enriched mRNA showed upregulation of genes associated with the glutamatergic M1 and M7 hdWGCNA modules that were broadly upregulated across glutamatergic subtypes in the snRNA-seq data (**Supplement**), validating relevance of these broad DEMs. GO terms associated with L2/3 IT enriched upregulated M4 and M9 modules associated with mitochondrial energetics were among the strongest bulk RNA-seq upregulated GSEA hits across conditions. Finally, for the ASD and neuropsychiatric-associated synaptosomal-specific downregulated *Dlg2* gene[63–66], which encodes the PSD93 excitatory synaptic scaffold protein, we validated reduction at the protein level in synaptosomal preparations (**Figure 4F-4H**). These results solidify transcriptional pathology in adult cortex due to *Chd8* haploinsufficiency and provide insights into cell-autonomous effects in post-mitotic excitatory neurons and suggest differential mRNA levels are driven by both transcriptional and post-transcriptional mechanisms that have heightened impact on synaptosomal mRNA levels.

Altered excitatory neuron spine dynamics and calcium signaling coherence in Chd8$^{+/-}$ *mice*

The snRNA-seq and bulk RNA-seq both pointed to cortical excitatory neuron dysfunction and previous studies have identified electrophysiological signatures in vivo and in vitro in glutamatergic neurons[21,36,37,40,40,41]. To further investigate structural pathology of cortical neurons, we crossed *Chd8*$^{+/-}$ mice with thy1-YFP mice, which express cytoplasmic yellow fluorescent protein in a sparse subset of layer 5 pyramidal neurons (L5 PyrNs)[67], and performed in vivo two-photon (2P) imaging on apical

327 dendrites of L5 PyrNs. We compared the density and dynamics of dendritic spines (postsynaptic
328 structure of majority excitatory synapse) between WT and *Chd8*$^{+/-}$ littermates at adolescence (P30) and
329 adulthood (P90) mice (**Figure 5A**). Adolescent *Chd8*$^{+/-}$ mice had lower spine density on the apical
330 dendritic tufts of L5 PyrNs (**Figure 5B**). Following the same dendritic segments over seven days, we
331 also found that *Chd8*$^{+/-}$ mice had increased dendritic spine formation relative to WT mice, but
332 comparable spine elimination (**Figure 5C**). On the other side, adult *Chd8*$^{+/-}$ mice had normal spine
333 density and dynamics (**Figure 7D-E**). These results indicate that *Chd8* haploinsufficiency delays
334 spinogenesis of cortical neurons during early development (before P30).

335

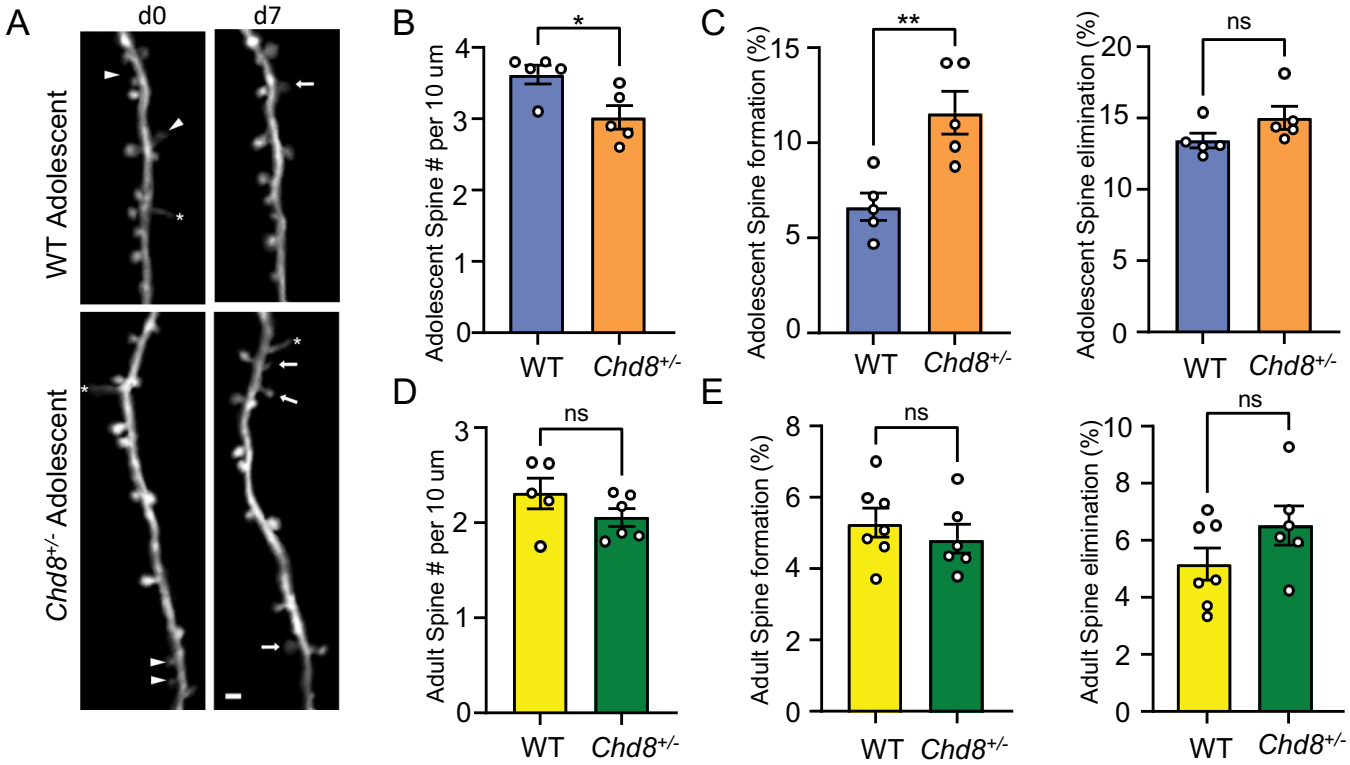

336

337 **Figure 5: Delayed spinogenesis during *Chd8*$^{+/-}$ development.** A) Dendritic segment imaged over 7-
338 days in somatosensory cortex of adolescent WT and *Chd8*$^{+/-}$ mice. Arrowheads: eliminated spines;
339 arrows: formed spines; asterisks: filopodia. Scale bar = 2 µm. B, D) Spine density in adolescent (b) and
340 adult (D) *Chd8*$^{+/-}$ or WT littermates. C, E) The percentage of spines formed or eliminated over 7d is higher
341 in adolescent (D) and adult (E) *Chd8*$^{+/-}$than WT littermates, mean, SEM., unpaired t-test. **p<0.01.

To understand how disruption of *Chd8* signaling affects the function of a cortical microcircuit, we performed calcium imaging in acute slices taken from wildtype or *Chd8*$^{+/-}$ mouse brains expressing the genetically encoded calcium indicator *GCamp6f* in prefrontal cortex neurons under the control of the human *Synapsin* promoter (**Figure 6A-D**). We collected 60-minute recordings from a total of 544 neurons from 8 wildtype slices (68+/-9 neurons/slice) and 818 neurons from 10 *Chd8*$^{+/-}$ slices (82+/-9

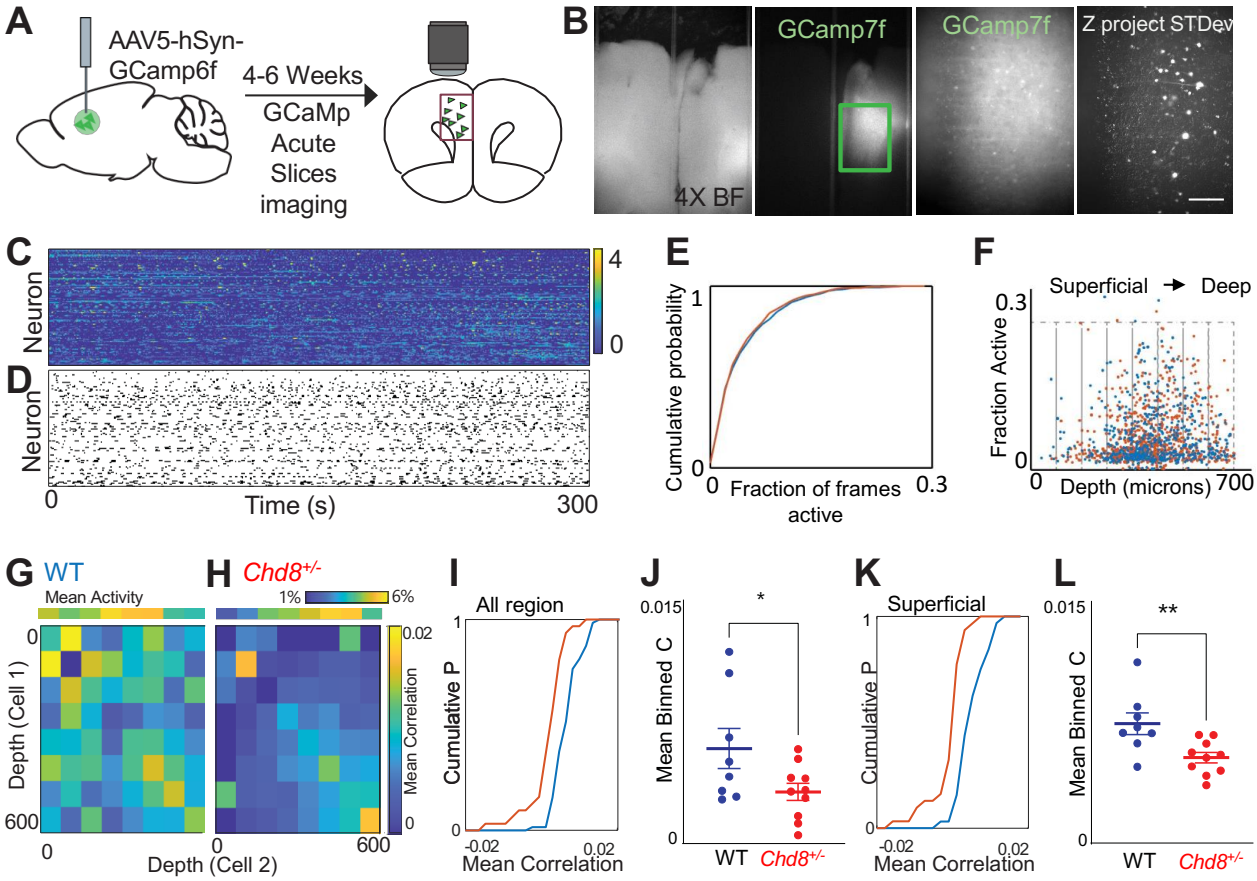

Figure 6: Disruption of coordinated activity in *Chd8*$^{+/-}$ PFC microcircuits. A. Mice injected with *Syn-GCamp6f* and activity recorded from acute slices after 4-6 weeks. B, wide field and GFP at 4x (left). 10X of individual neurons and z-projection of standard deviation across frames (right). C, z-scored fluorescence traces from neurons in a single slice. D, Raster of events. E, Cumulative probability function showing overlap in fraction of frames active for neurons from WT (blue) and *Chd8*$^{+/-}$ (red) slices. F, Activity of each cell as a function of depth from cortical surface. Cells binned by distance from surface (gray boxes) and mean correlations within and between bins calculated. G,H, 8x8 matrix of mean correlation coefficient calculated for cells within each pair of bins, averaged for WT (G) or *Chd8*$^{+/-}$ (H) slices. I, cumulative distribution function (CDF) of mean correlation across 544 pooled WT (blue) neurons and 818 pooled *Chd8*$^{+/-}$ (red) neurons for all bins. J, Mean correlation coefficient of WT and *Chd8*$^{+/-}$ slices ($p < 0.05$, t-test). K, CDF of the mean value of the subset of bins in which neuron 1 was < 300 microns from cortical surface. L, Mean correlation coefficient of superficial neurons in WT and HET slices ($p < 0.01$, t-test).

361 neurons/slice). Overall, the activity of wildtype and *Chd8*$^{+/-l}$ slices was similar (**Figure 6E-F**; mean
362 fraction of frames active = 5.2+/-0.2% WT vs 5.0+/-0.2% HET, p = 0.4, t-test). To examine the
363 functional connectivity across the prefrontal microcircuit, we binned neurons into eight 75 μm bins
364 starting at the cortical surface and extending to a depth of 600 μm, and calculated the correlation
365 coefficient between the activity of neurons according to the location of each neurons within the slice,
366 then averaged the correlation coefficient based on the depth of 600 μm, and calculated the correlation
367 coefficient between the activity of neurons according to the location of each neurons within the slice,
368 then averaged the correlation coefficient based on the position of each neuron in the cell pair (**Figure**
369 **6G-H**). Visual examination of the resulting matrix of averaged correlations revealed that neuron pairs
370 from heterozygous *Chd8*$^{+/-l}$ slices had on average lower correlation coefficients compared to neuron
371 pairs from WT slices, and this was particularly pronounced when at least one neuron was located in the
372 superficial (< 300 μm from the cortical surface) aspect of the slice (**Figure 6I-L**; mean correlation
373 coefficient WT 0.0057 +/-0.0001 vs 0.0030+/-0.0005, $p < 0.05$, t-test; n = 8 WT and 10 HET slices;
374 mean correlation coefficient superficial WT 0.0050+/-0.0009 vs HET 0.0021+/-0.0004, $p < 0.01$, t-test; n
375 = 8 WT and 10 HET slices), suggesting that these neurons are relatively disconnected from deeper
376 layer neurons in the prefrontal microcircuit of mutant *Chd8*$^{+/-l}$ animals.

377 *Chd8*$^{+/-}$ *mice exhibit disrupted sleep*

378 We previously tested *Chd8*$^{+/-}$ mice across a battery of behavioral assays, finding deficits in novel object
379 recognition and fear conditioning in the learning and memory domain with no differences in sociability
380 using the three-chamber social preference test or in male-female interactions. Sleep issues are a
381 common symptom in humans with *CHD8* mutations and the transcriptional dysregulation in *Chd8*$^{+/-}$
382 mice featured upregulation of the circadian-associated M7 glutamatergic module. Thus, we used
383 EEG/EMG to continuously record neural activity during a 24-hour period, assigning states of REM,
384 NREM, and Wake, analyzing 11 *Chd8*$^{+/-}$ (female=7, male=4) and 8 WT littermates (female=4, male=4)
385 (**Figure 7A-B'**). The total time in seconds that each mouse spent in each state was calculated for each
386 hour (**Figure 7C-D**). For comparison of sleep patterns, total and standard deviation (SD) were

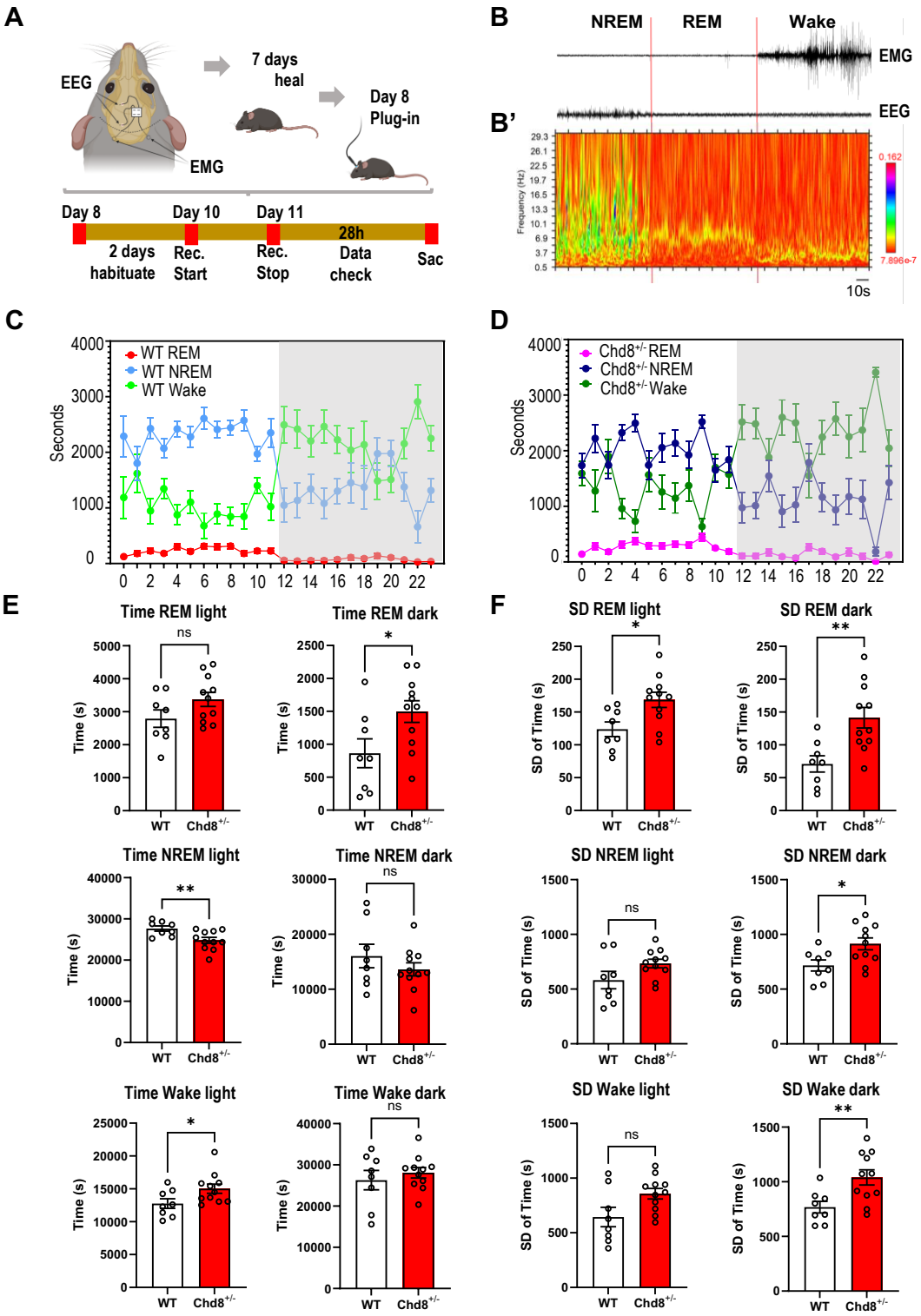

Figure 7: Perturbed sleep patterns in *Chd8*$^{+/-}$ mice. A) Schematic of 24hr EEG/EMG sleep analysis. B) Example EEG/EMG traces showing activity during REM, NREM, and Wake state. B') Spectrogram of the EEG signal in B C) Summary of time spent in each state during each hour of the 24hr monitoring period for wild type (left) and *Chd8*$^{+/-}$ groups. Mean and SD shown. D) Summary of mean total time spent in each state separated by light and dark stages (left). Summary of SD in time spent in each state separated by light and dark stages. See text for statistical summary.

394 calculated by subject using hourly values and compared for light (Zeitgeber Time ZT0-ZT12) and dark
395 (ZT12-ZT24) phases (**Figure 7E-F**). *Chd8*$^{+/-}$ mice had a significant increase in time spent in REM in the
396 dark stage (P = 0.036 [unpaired t-test with Welch's correction]), and significantly less time spent in
397 NREM (P = 0.008 [unpaired t-test with Welch's correction]) and increased time spent in wake state (P =
398 0.040 [unpaired t-test with Welch's correction]) in the light phase. Comparing SD of the time spent per
399 state across hours, *Chd8*$^{+/-}$ mice showed higher variability in all states. SD of REM time was
400 significantly higher during both light and dark phases (P = 0.012 and 0.003, respectively), and SD of
401 NREM and Wake time were significantly higher during dark phase (P-values = 0.017 and 0.006,
402 respectively) and marginally increased during the light phase (P = 0.115 and 0.059 respectively).
403 Together results revealed disrupted sleep patterns in *Chd8*$^{+/-}$ mice, including more time in REM and
404 time spent in Wake in the light stage, and higher variability in time spent in specific sleep/wake states
405 across the light and dark stages.

406 **Discussion**

407 This study extends understanding of how *Chd8* haploinsufficiency alters the adult mouse cerebral
408 cortex. Via stereology and snRNA-seq, we show that increased cortical volume in *Chd8*$^{+/-}$ mice is not
409 due to increase in cortical excitatory neuron numbers, and, in fact, is associated instead with decreased
410 neuron density. While macrocephaly was not due to increased numbers in excitatory neurons, these
411 cells do exhibit sensitivity to *Chd8* haploinsufficiency at the level of cell-type specific transcriptional
412 pathology, synaptosomal RNA homeostasis, dendritic spine formation, and signaling coherence.
413 Finally, we expand the phenotypic testing of heterozygous *Chd8* mouse models in the domains of sleep
414 and cognitive performance, finding perturbations to sleep state that aligns with high prevalence of sleep
415 disturbance reported in patients carrying *CHD8* mutations. Overall, our findings add to the
416 understanding of the effects of heterozygous *Chd8* mutation on the mouse cortex, providing new
417 insights into anatomical, cellular, and circuit impacts, dosage sensitivity during brain development and
418 in post-natal postmitotic neurons, and demonstrating presence of sleep disturbance.

419 Increased brain size during development and increased cortical volume in adult mice has been reported
420 across different mutant *Chd8* mouse lines[20,25,27,29]. *Chd8* haploinsufficiency has also been linked to
421 altered neurogenesis in mouse[20,25,28] and in vitro in human cellular and organoid brain models[32,38].
422 While increased production of cortical excitatory neurons during development leading to increased
423 neurons in the adult cortex seemed a plausible explanation for cortical volume increase, results from
424 both stereology and snRNA-seq show this to not be the case in our *Chd8*$^{+/-}$ mouse model. In fact, we
425 found the opposite pattern of decreased excitatory neuron density driven by increased volume without
426 increased neuron counts or increased soma size. There was a trend of decrease in proportions of
427 certain glutamatergic types in snRNA-seq data, reaching significance for decreased in L6 IT neurons in
428 the mutants. snRNA-seq indicated significant increase in proportion of OPCs and trend towards
429 increase in astrocytes, raising the possibility that increased proportions of non-neuronal cells may
430 explain some of the increased cortical volume. Whatever the roots of *Chd8*-associated macrocephaly, it
431 is unclear what the link between this neuroanatomical signature and relevant social and cognitive
432 phenotypes, with a recent study finding little correlation between adult brain weight and behavioral
433 phenotypes for *Chd8*$^{+/-}$ mice from a series of genetic backgrounds[34]. It could be that causes of
434 macrocephaly and behavioral phenotypes in *Chd8*$^{+/-}$ mice are independent, or that the mechanisms for
435 are linked, but with variable anatomical and behavioral outcomes in adult mice. Our results do point to
436 glutamatergic pathology and one intriguing possibility is that changes in neuronal morphology and
437 microstructure organization, for example dendritic arborization, could account for the changes. Further
438 studies will be needed to resolve specific causes of volume increase in *Chd8*$^{+/-}$ adult cortex.

439 Via unbiased snRNA-seq, we found that glutamatergic neurons exhibit the strongest transcriptional
440 pathology across cell types in adult mouse *Chd8*$^{+/-}$ cortex, with the most extensive impacts in L2/3 IT
441 and L4/5 IT subtypes. We identified subtype-specific and shared glutamatergic DEMs, including shared
442 upregulation of M1 and M7 modules, which are associated with general neuron-associated pathways
443 and with specific circadian rhythm GO terms. Transcriptional pathology in bulk RNA-seq analysis of
444 constitutive and conditional *Chd8*$^{+/-}$ mutants here aligns with *CHD8* studies in vitro and using mouse

445 models[12,20,22,24,25,28,68], with our study adding substantially via integrating single cell and bulk, constitutive
446 and conditional mouse models, and synaptosomal mRNA fractions. These findings include upregulated
447 aerobic respiration and mitochondrial energetics, which we map to having the strongest signature in
448 L2/3 IT neurons, and downregulation associated with synaptic organization and signaling. Bulk RNA-
449 seq transcriptional changes in excitatory neuron-specific *Chd8*$^{+/flox}$ mice paralleled changes in
450 constitutive heterozygous *Chd8*$^{+/-}$ mutants, demonstrating continued requirement for full *Chd8* dosage
451 and indicating that excitatory neuron transcriptional phenotypes in mature *Chd8*$^{+/-}$ mice may be
452 independent of developmental impacts. Our findings of effects in *Chd8*$^{+/flox}$ mice due to ablation in
453 excitatory neurons are consistent with earlier in vitro studies of both heterozygous and homozygous
454 neuronal ablation[40,69], and extend previous studies of adult *Chd8*$^{-/-}$ conditional mutant mice that did not
455 examine NDD-relevant heterozygous mutants[44]. We further link transcriptional dysregulation in
456 glutamatergic neurons to functional impacts in these cells, finding altered dendrite spine formation
457 during adolescence which manifests at the circuit level as de-correlated spontaneous prefrontal activity.
458 Finally, though not directly linked to specific cells or circuits, we identified perturbed sleep patterns
459 *Chd8*$^{+/-}$. These findings are highly relevant to NDDs, as disrupted synaptic development and altered
460 network activity represent candidate causal mechanisms and sleep disturbances are commonly
461 reported in individuals with ASD and related conditions[70] and are one of the more penetrant phenotypes
462 in CHD8-NDD[71]. Constitutive *Chd8*$^{+/-}$ mice do not exhibit classic sociability deficits in the three-chamber
463 social preference assay and behavioral and cognitive phenotypes vary across *Chd8*$^{+/-}$ studies and
464 across mouse genetic backgrounds[20–22,24,25,27,34,37]. As such, behavioral studies of *Chd8* mutant mice
465 have proved challenging to interpret. Our results, along with studies that have identified other
466 phenotypes at cellular, molecular, and anatomical level such as via electrophysiology or structural MRI,
467 highlight molecular endophenotypes that may be more consistent in expression and have high
468 translational relevance. Future studies will be needed to determine which aspects of *Chd8*$^{+/-}$ mouse
469 phenotypes are driven by developmental versus later requirement for full dosage, which specific
470 neuronal and glial populations are dependent on Chd8, and if molecular, cellular, and neuroanatomical
471 phenotypes are consistent between mutant lines and across mouse and human *CHD8*$^{+/-}$ models.

472 One novel finding from our study was the significant differences in DE signatures between nuclear and
473 synaptosomal mRNA preparations. Bulk nuclear RNA-seq recapitulated upregulation observed for the
474 two glutamatergic DEMs with broad dysregulation and had the highest concordance with snRNA-seq
475 DEGs, as well as being strongly concordant with the full bulk cortex RNA-seq. Thus, nuclear RNA
476 changes observed at both single cell/nucleus and bulk level appear robust. Surprisingly, there was
477 relatively weak concordance between synaptosomal and nuclear DEGs, with a stronger overall DE
478 signature in the synaptosomal enriched preparations. These findings indicate disconnect between
479 changes in transcriptional rate, captured by nuclear RNA datasets, and changes in steady-state mRNA
480 levels in *Chd8*$^{+/-}$ cortex. We and others previously identified altered mRNA splicing in *Chd8*$^{+/-}$ mouse
481 and *in- vitro* models[20,72], raising the possibility that *Chd8* haploinsufficiency directly or indirectly alters
482 RNA processing. ChIP-seq studies of CHD8 have consistently identified enrichment of regulatory
483 targets associated transcription and RNA processing[73]. Intriguingly, we did observe down-regulation of
484 RNA processing associated with L4/5 IT specific DEM M6. Beyond a better understanding of the
485 molecular function of Chd8, future studies are needed to determine whether the synaptosomal DEG
486 signature is specific to synaptosomal localized mRNA, or a more broadly present in cytosolic mRNA
487 overall, what the cell-type specific impacts are on mRNA processing and localization, whether
488 synaptosomal RNA differences are associated with differences in synaptic protein makeup and synaptic
489 function, and if this finding extends to *CHD8*$^{+/-}$ human neurons.

490 There are limitations to this wok that should be considered. The number of replicates (N=5 per
491 genotype) and contrasts (*Chd8*$^{+/5bpdel}$ versus WT) was restricted for snRNA-seq, somewhat limiting
492 statistical power and scope of these experiments. Additionally, nuclei-based methods may miss
493 changes in cytosolic mRNA levels[74,75], which may be relevant based on our bulk analysis. Further,
494 there are challenges with snRNA-seq for DE testing at single gene level using individual cells/nuclei.
495 While Wilcoxon tests are commonly used in single cell differential expression analysis, we found this
496 method yielded high false positive rates (as issue that has been raised previously[76]. In contrast,
497 pseudobulk and hdWGCNA methods take advantage of aggregating cells or genes to compare

498 expression at the cluster or module level, giving more robust DE results at the cost of reducing
499 resolution for single cell and single gene level effects. Finally, it is unclear how much the transcriptomic
500 pathology extends to protein level or impacts function. With regard to functional studies, we chose three
501 *in vivo* assays to focus on: spine dynamics, correlated GCaMP signaling, and sleep. Previous studies
502 have not tested these phenotypes, and we believe our results provide new insights into pathology.
503 However, other assays would be valuable and each of the domains we studied could be investigated at
504 higher depth. We did not test conditional *Chd8*$^{+/flox}$ mice beyond bulk RNA-seq, leaving unanswered
505 whether this model recapitulates other pathology. Finally, *Chd8* mutant mouse lines exhibit variation in
506 phenotype penetrance and expressivity, which is at least in part due to the impact of genetic
507 background[34]. Considering this, our findings may not be conserved in other *Chd8* mouse models,
508 though we note overlapping transcriptional signatures described here and in other studies as
509 summarized above. While these limitations hold, our results lay the foundation for future work
510 characterizing constitutive and conditional mutant *Chd8* mouse models.

511 Our study extends understanding of the impacts of Chd8 haploinsufficiency in vivo in mouse brain, with
512 a focus on glutamatergic excitatory neurons. We show that constitutive and conditional heterozygous
513 ablation leads to convergent transcriptional pathology and to impacts on neuronal spinogenesis and
514 circuit function. Our findings illustrate how loss of *Chd8*, which has received attention for high
515 expression in early development and role as a chromatin remodeler, impacts the cell-type specific
516 makeup and pathology of the adult cortex extending across molecular, cellular, circuit, and organismal
517 phenotypes and providing support for a framework where excitatory neuron dysfunction at the level of
518 synapses and circuits may be an area of casual convergence in monogenic NDDs featuring ASD and
519 ID and raising the possibility that interventions targeting postnatal postmitotic cortical neurons may be
520 effective at addressing at least some of the underlying NDD pathology.

521

522 **Acknowledgements**

523 This work was supported by the National Institutes of Health National Institute of Mental Health (NIH
524 NIMH) R01 MH120513 to A.S.N., National Institute of Neurological Disorders and Stroke (K08
525 NS105938-01A1 to NAF), the Simons Foundation (Award # 604325) and the National Institute of
526 Mental Health (R01MH117961 to VS), as well as the UCSF Dolby Family Center for Mood Disorders.
527 C.P.C was supported by the NIH NIMH Autism Research Training Program fellowship (T32 MH073124-
528 16). A.A.W was supported by NIH NIMH F31 MH119789 and T32 GM007377. We thank Dr. Wenjie
529 Bian and Dr. Luis de Lecea at Stanford University, for their technical advice on EEG/EMG experiments
530 and data analysis.

531 **Author contributions**

532 A.S.N. conceived the project with substantial contributions from Y.Z., D.A., V.S. C.P.C led the project
533 execution, designed experimental work and oversaw most aspects of data generation and analysis. S.L
534 fully executed snRNA-seq bioinformatic and led most of the data analysis with contributions from K.C,
535 N.S, E.F, N.C., E.S., C.A., A.W and A.S.N. C.P.C, W.A, J.B, and S.F carried out experimental
536 stereology and analysis. C.P.C, S.L, P.B, A.K.S, D.P, D.R, M.C, L.D, J.Z and R.O carried out
537 experiments. C.M. and J.B. performed 2P spine imaging and analysis, J.S., B.M, and J.L. performed
538 EEG recording and analysis. CPC, SL and ASN wrote the manuscript.

539

540 **Methods**

541 **Animals**

542 Generation of Cas9-mediated 5bp frameshift deletion in exon 5 of *Chd8* in mice (here referred to as
543 *Chd8*$^{+/-}$ mice) was previously described[20]. For in vivo imaging, this mouse line was crossed with the
544 thy1-YFP-H (JAX strain: 003782) mouse line and maintained in the C57BL6/J (JAX strain: 000664)
545 background. Mutant mice *Camk2a-CRE Chd8*$^{+/flox}$ were obtained by crossing Chd8 loxP mice on

546 C57BL/6J (*Chd8*^{em3Lutzy}; JAX strain: 031555) to Camk2a-CRE (*B6.Cg-Tg(Camk2a-cre)T29-1Stl/J*; JAX
547 strain: 005359) to achieve heterozygous ablation in post-mitotic forebrain glutamatergic neurons. All
548 protocols utilized in the generation of mouse brain samples were approved by the Institutional Animal
549 Care and Use Committees (IACUC) at the University of California Davis and University of California
550 Santa Cruz. Mice were housed in a temperature-controlled vivarium maintained on a 12-h light–dark
551 cycle. We made efforts to minimize pain, distress and the number of animals used in the study.
552
553 **Histological tissue preparation and Nissl Stain**
554 Thirty-six 42-day-old mice were included in this analysis (16 brains per genotype, 16 per sex).
555 Mice were anesthetized using Isoflurane and perfused transcardially using room temperature saline
556 solution (0.9% NaCl) followed by 4% paraformaldehyde (PFA) in 0.1 M phosphate buffered (PB) saline
557 using a peristaltic pump (Minipuls 3, Gilson) at 20 rpm flow rate. Brains were removed and post-fixed in
558 4% PFA at 4ºC for 24 h. Fixed brains were cryoprotected in 50 ml of 10% and 20% glycerol solutions
559 with 2% DMSO in 0.1 M phosphate buffer (PB; pH 7.4; for 24 and 72 hours, respectively). Brains were
560 blocked at -2.00mm posterior to the interaural line prior to flash freezing. Sections were cut using a
561 freezing, sliding microtome in 4 series at 60 µm (Microm HM 440E, Microm International, Germany).
562 Every 4th section was collected in 10% formaldehyde in 0.1 M PB (pH 7.4) and post-fixed at 4ºC for 1
563 week[77]. Sections were rinsed twice for 1 hour each in 1ml of 0.1M PB, mounted on gelatin-coated
564 slides, and air-dried overnight at 37°C. Defatting was performed in a mixture of chloroform/ethanol (1:1,
565 vol) for 2 x 1 hour. The brains were rehydrated in graded alcohols; 100% ethanol, 100% ethanol, 95%
566 ethanol, 70%, 50% and dipped in deionized water[77,78]. Sections were stained 40 seconds in a 0.25%
567 thionin solution (Fisher Scientific, Waltham, MA, cat. no. T-409), dehydrated through graded alcohols,
568 differentiated in 95% ethanol and 5 drops of glacial acetic acid, cleared in xylene and cover-slipped with
569 DPX (BDH Laboratories, Poole, UK)[77].
570
571 **Stereology**

572 The inferior boundary of the cortex was defined as the bottom of the agranular insular area (AIA), and
573 the superior boundary was defined as the anterior cingulate area (ACA) or the retrosplenial area (RSA)
574 and the white matter was then followed to the ACA/RSA border[79]. Neuron number, neuronal soma size,
575 and brain volume were estimated using Stereoinvestigator V10.50 (MBF Biosciences, Williston, VT)
576 attached to a Zeiss Imager.Z2 Vario with a Zeiss AxioCam MRc. An EC PlanNeoFluar 2.5 x objective
577 was used to trace the outline of the cortex and a PlanApoChromat 100x oil objective was used for cell
578 counts and soma size determinations. The volume of the cortex was determined using the Cavalieri
579 method[53,54,80]. For each mouse, 15-18 sections (480 µm apart) were analyzed with the first section
580 chosen randomly amongst the first through the cortex. Estimates of neuron numbers were obtained
581 using the Optical Fractionator method[55,81]. Since no lateralization was found in the volumetric estimates
582 ($p = 0.65$), we sampled the left hemisphere of half of the mice and the right hemisphere of the other half
583 for estimates of neuron numbers. We used the same sections that were used for volumetric estimates.
584 We used a counting frame size of 18x18x10µm with 2 µm guard zones, and a scan grid of 480x480 µm
585 placed at a random angle. Neurons were defined following established protocols[53–55,80–82] based on: 1)
586 dark staining, 2) a well-defined nucleolus and 3) a round, non-jagged cell body[77,82–85]. Section thickness
587 was measured at every counting site. The volume of neuronal somas was determined using the
588 Nucleator method[86] during the Optical Fractionator analysis. Comparison of stereological measures
589 (volume, neuron number, and soma size) were performed via ANOVA to examine global effects of sex
590 and genotype and test for sex by genotype interaction, and then via t-test to compare the effect of
591 genotype in males and females. In addition to test results, effect sizes are reported for ANOVA (partial
592 eta squared, η_p^2) and t-test (Cohen's d). Statistical analyses were performed using SPSS (version 26),
593 plots were generated using *ggplots2* package in R programming language[87].
594
595 **Rostro-Caudal Volume analysis.**
596 To investigate the effects of genotype and sex on Cavalieri counts, mixed-effects regression models
597 were employed using the `lme4` and `lmerTest` packages in R. The initial model tested the main effect
598 of genotype on Cavalieri counts while accounting for sex, batch effects, and the z-position of the mouse

599 brain sections. Polynomial terms up to the fourth degree for z-position (Zpos) were included to capture
600 potential non-linear relationships observed in exploratory data analysis. Subsequently, a model was
601 fitted to examine the interaction between genotype and sex, including an interaction term for these
602 variables. This model was structured to evaluate whether the effect of genotype on Cavalieri counts
603 varied by sex. The analysis was extended to assess the effects of genotype across different rostral-
604 caudal brain segments. The segments - Rostral, Median, and Caudal - were defined based on changes
605 in direction observed in the z-position plot, aiming to reflect the anatomical structure of the mouse brain.
606 Dummy coding was applied to compare each segment against the reference levels. The final model
607 included these segments as factors, alongside the previously mentioned covariates and polynomial
608 terms for z-position. For data visualization, the `ggplot2` package was utilized to create plots depicting
609 the relationship between z-position and Cavalieri counts. Separate smoothed plot lines were generated
610 for each sex and genotype combination, providing a clear visual representation of the data across
611 different brain regions. All statistical analyses were performed using R. The mixed-effects models
612 allowed for robust estimation of fixed effects while accounting for random effects associated with batch
613 and individual mouse variations.
614

615 **Adult mouse cortex dissections**

616 Mice were anesthetized with isoflurane and euthanized via cervical dislocation in accordance with
617 institutional animal care protocols. Brains were rapidly extracted, and cerebral cortices were dissected
618 on ice following standard anatomical landmarks. Dissected tissues were snap-frozen in liquid nitrogen
619 or dry ice to preserve molecular integrity and minimize RNA degradation, and stored at -80°C until
620 further use. These samples were subsequently used for RNA extraction, nuclear isolation, or cellular
621 fractionation, as described below.
622

623 **Cellular Fractionation (synaptosomal preparation)**

624 Brains from *Chd8*$^{+/5bpdel}$ and wild-type littermates were collected on or around PND60. Following
625 cervical dislocation, brains were sub-dissected to isolate Cortex. Flash frozen cortices were stored at -

626 80C until further processing. On the day of cellular fractionation, samples were treated with Syn-Per
627 reagent (ThermoFisher Scientific Catalog #87793) to obtain cytosol, synaptosome and flowthrough
628 ("total") fractions. The "total" fraction was then used treated with "NE-PER™ Nuclear and Cytoplasmic
629 Extraction Reagents" (cat #78833) to obtain the nuclear, and a "cleaner cytosol" fractions. Total RNA
630 from these fractions was then extracted using RNA RNAqueous™ Total RNA Isolation Kit (cat#
631 AM1912 ThermoFisher Scientifics). Manufacturer protocols were followed with minor adjustments to
632 increase RNA yield from cellular fractions. Adjustments included combining the cortex samples with
633 500µl of Syn-Per reagent and 5µl of protease inhibitors during homogenization, based on our starting
634 sample amount, and adding 350µl of RNA extraction lysis buffer immediately after fractionation to the
635 synaptosome and nuclear fractions.
636
637 **Western blot analysis**
638 Synaptosomal fractions were obtained from cortical extracts from PND 60 micethe using the Syn-Per
639 reagent following manufacturer instructions as described above. Protein concentration was quantified
640 using a BCA protein assay kit (Pierce, 23225) and samples were stored at -80℃ until use. For the SDS
641 gel electrophoresis, samples were diluted in 6X Laemmli SDS buffer (375mm Tris-HCl, 9% SDS, 50%
642 glycerol, 0.03% Bromophenol blue) and 5% β-mercaptoethanol, boiled at 70℃ for 10 min, and
643 separated on a 4-20% polyacrylamide tris-glycine protein gel (BioRad). Prior loading into the gel,
644 samples were incubated at 70℃ for 10 min. After SDS-PAGE, proteins were wet transferred onto a
645 PVDF membrane (Millipore Sigma) overnight at 4℃ (13mA, constant current). Membranes were
646 blocked with Intercept PBS blocking buffer (Li-Cor) at room temperature for one hour. Primary antibody
647 PSD93 (1:50, DSHB, Clone N18/28, supernatant fraction) was diluted in 7.5 ml Intercept PBS blocking
648 buffer with 0.1% Tween. Membranes were incubated with the primary antibody solution overnight at
649 4℃, then washed four times for 10min with PBS with 0.1% Tween (PBST). Fluorescently tagged
650 secondary antibody (Li-Cor) were diluted in 10ml Intercept PBS blocking buffer with 0.1% Tween. After
651 the initial washes, blots were incubated with the secondary antibody solution for one hour at room

temperature. Blots were washed an additional four times for 10min with PBST and two times with PBS. Bands were visualized using the Odyssey DLx imaging system (Li-Cor).

RNA Isolation, bulk RNA-Sequencing and bioinformatics analysis

Mouse cortices were collected at around PND60 from the following groups: 16 wild-type (WT) mice and 16 *Chd8*$^{+/-}$ mice (8 males and 8 females in the WT group; 7 males and 9 females in the *Chd8+/-* group), as well as 6 WT and 8 Chd8+/flox control mice (4 males and 2 females in the WT group; 5 males and 4 females in the *Chd8*$^{+/flox}$ group). Samples were snap frozen on dry ice and stored at -80C until RNA preparation. Total RNA was obtained using RNAqueous Total RNA Isolation Kit (cat# AM1912 ThermoFisher Scientifics), and assayed via Agilent RNA 6000 Nano Bioanalyzer kit/instrument. Sample RIN scores ranged from 8 to 9.4. Poly-A-enriched mRNA libraries were prepared at Novogene using Illumina reagents. Libraries were sequenced using Illumina NovaSeq 6000 S4 system, paired-end 150 (PE150) method. Reads were aligned to mouse genome (GRCm38/mm10) using STAR (version 2.5.4b)[88], and gene counts were produced using featureCounts[89]. On average, 50 million paired-end reads (PE) aligned per sample, with a range of 32 to 84 million reads. Data quality was assessed using FastQC[90], and principal component analysis (PCA) was used to determine presence of sample outliers. All 24 samples were qualified for the analysis. Raw RNA-seq fastq files and a gene count matrix is available on GEO (accession number TBD). Bioinformatic analysis was performed using R programming language version 4.2.1 (R Development Core Team, 2015) and RStudio integrated development environment version 2023.06.0 (Team R, 2018). Plots were generated using ggplot2 R package version 3.4.0. Heatmaps were generated using pheatmap R package 1.0.12.

Bulk differential expression (DE) analysis

For DE analysis we used edgeR R package[91]. Genes with a minimum of 1 counts per million (CPM) in at least six samples were included in the analysis. The first surrogate variable from the SVA-batch-correction method was used as a covariate in the edgeR GLM model[92]. For sex-stratified DE, we used a threshold of CPM > 1 in at least 3 samples, and no batch correction. Reads Per Kilobase per Million

679 mapped reads (RPKM) were used for plotting summary heatmaps and expression data of individual
680 genes.
681
682 **Bulk gene ontology enrichment analysis**
683 To test for enrichment of GO terms we used the TopGO R package version 2.34[71]. Mouse Gene
684 Ontology (GO) data was downloaded from Bioconductor (org.Mm.eg.db). For the analysis presented
685 here, we restricted our testing to GO Biological Process annotations and required a minimal node size
686 of 20, and at least 2 significantly DE genes in a GO term. We used the internal 'weight01' testing
687 framework and the Fisher exact test, a strategy recommended for gene set analysis that generally
688 accounts for multiple testing comparisons. For GO BP analysis, we reported terms with p-value<0.05.
689 For all enrichment analysis, the test set of DE genes was compared against the background set of
690 genes expressed in our study based on minimum read-count cutoffs described above.
691
692 **Single Nuclei RNA-seq**
693 **Nuclei isolation for snRNA-seq and pooling strategy**
694 Frozen issue from the first 6 samples was processed into nuclei using 2mL glass dounce homogenizers
695 containing 2mL of EZ Prep lysis buffer each. Tissue for 3 samples was dounced over ice, 25 times with
696 pestle A and 35 times with pestle B. Each solution was transferred to a 15 mL conical tube, then the
697 same douncing process was repeated for the second set of 3 samples. Solutions from the latter 3
698 samples were pooled with those of the first 3 such that each pool contained one male and one female
699 of opposite genotype. An additional 6 mL of EZ Prep lysis buffer was added to each conical tube and
700 the tubes were incubated on ice for 5 minutes. Homogenates were centrifuged at 500xg for 5 minutes
701 at 4°C, the supernatant was discarded, and the pellet was washed twice in NSB (1X PBS with 0.01%
702 BSA and 0.1% RNAse inhibitor). The final pellet was resuspended in 1mL NSB then passed through a
703 20uM cell strainer. Nuclei were counted using a LUNA-FL cell counter and Acridine Orange/ Propidium
704 Iodide stain. The 10X Genomics nuclei isolation kit, with protocol as described, was used to isolate
705 nuclei for the final 4 samples. These samples were combined into 2 pools, each containing one male

706 and one female of opposite genotype, then nuclei were counted as described previously. Nuclei
707 suspensions had concentrations adjusted to target 10,000 nuclei for sequencing per pool, then used as
708 input for the 10X Genomics 3' Gene Expression Assay. Libraries were generated according to the v3
709 protocol by the UC Davis DNA Technologies Core. For the first 3 pools, libraries were sequenced with
710 the Illumina NovaSeq 6000 at 80,000 reads per nucleus. The remaining two pools were sequenced with
711 the Element Biosciences AVITI at 80,000 reads per nucleus.
712
713 **RNA-seq relevant bioinformatics**
714 **Pre-processing of snRNA-seq data and initial QC**
715 De-multiplexed sequencing data were obtained from the UC Davis DNA Technologies Core as FASTQ
716 files. FASTQ files were passed through the Cell Ranger *count* pipeline for alignment to the mouse
717 mm10 genome, filtering, and creation of feature-barcode matrices. Ambient RNA removal was
718 performed using SoupX (version), and Seurat objects were generated using Seurat (version). These
719 Seurat objects were subjected to initial clustering, and each resulting cluster was filtered based on
720 cluster-specific thresholds for UMI count, feature count, and percentage of mitochondrial reads, which
721 were determined using standard deviation criteria. Mitochondrial genes were then removed from all
722 objects.
723 **Doublet removal**
724 The DoubletFinder package (version) was used to assign nuclei as 'Singlet' or 'Doublet'. Predicted
725 doublets were removed before proceeding with downstream analyses.
726 **Assigning sex and genotype**
727 Nuclei were next assigned as 'male' or 'female' using the sxreveal package, which uses X- and Y-linked
728 marker gene expression to predict sex. *Chd8* genotype was assigned based on the predicted sex and
729 pool-specific metadata. Because each pool consisted of only one male and one female of opposite
730 genotype, all female nuclei in a pool were assumed to be one genotype and all males were assumed to
731 be the other.
732 **Clustering analysis**

733 Seurat objects for each of the 5 samples were individually passed through *SCTransform* to normalize
734 counts, then all 5 were integrated using *IntegrateData*. The 'RNA' assay of the integrated object was
735 normalized and scaled using *NormalizeData* and *ScaleData*. Principal Components Analysis was
736 performed on the 'Integrated' assay of the integrated data to identify top variable genes, and
737 *FindNeighbors* was used to construct a KNN graph based on their euclidean distance in PCA space.
738 The data were then passed through *FindClusters* to group cells into clusters using the Louvain
739 algorithm. Clusters were visualized with uniform manifold approximation and projection (UMAP).

740 **Cell type annotation**

741 *FindAllMarkers* was used to identify cluster marker genes. Modules of cell type marker genes described
742 in published scRNA-seq datasets from adult mouse cortex were constructed. Canonical marker genes
743 were added to these modules, then *AddModuleScore* was used to calculate relative expression of each
744 module in each cluster. The cell type associated with the marker gene module that had the highest
745 expression in each cluster was assigned as that cluster's identity. All nuclei were assigned identities at
746 3 levels of classification, with 'Cell_Type_1' being the most specific and 'Cell_Type_3' the broadest.

747 **Cell type re-clustering**

748 Clusters that were poorly clustered, had a high percentage of mitochondrial reads relative to other
749 clusters, or had ambiguous marker genes (i.e. markers for multiple distinct cell types) were removed
750 before subsequent analysis. The filtered Seurat object was then re-normalized, re-scaled, and re-
751 clustered as described previously.

752 **Differential expression (DE) analysis**

753 A pseudo-bulk approach was used to identify differentially-expressed genes in each cortical cell
754 population. Each cluster was extracted as a subset of the main Seurat object, then raw counts were
755 passed through the *DESeq2* pipeline to compare *Chd8* mutant and wild-type nuclei within that subset.
756 Batch was included as a covariate in the *DESeq2* statistical model. DEGs with an adjusted p-value <
757 0.05 were deemed significant. This analysis was performed at each of the 3 levels of cell type
758 assignment.

759 **Burden analysis**

760 A minimum expression threshold was determined based on the minimum expression level (‘baseMean’)
761 of DEGs with p-value < 0.05. For each cell type, DE burden was calculated as the percentage of DEGs
762 relative to the total expressed genes that passed the minimum expression threshold. A permutation test
763 with 1,000 iterations was performed to assess the statistical significance of the observed DE burden.
764 This analysis was performed at each of the three levels of cell type classification.

765 **Cell type proportion analysis**

766 For each cell population, nuclei of each genotype were counted, then counts were converted to a
767 proportion of the total cells in each sample. Linear models adjusted for genotype, sex, and batch were
768 used to assess whether or not the proportions of mutant and wild-type nuclei for each cell type were
769 statistically different.

770 **hdWGCNA**

771 High-dimensional weighted gene co-expression network analysis (hdWGCNA) was applied to construct
772 gene co-expression networks for each cell population. Nuclei of specific cell types were grouped by
773 sample and passed through the *MetacellsByGroups* function to create metacells. Custom parameters
774 for 'k', 'max_shared', and 'min_cells' were chosen for each cell type. We determined the optimal soft
775 power using *TestSoftPowers*, built the co-expression network with *ConstructNetwork*, and detected
776 modules via hierarchical clustering. Harmonized module eigengenes (hMEs) were calculated for each
777 module using *ModuleEigengenes* and *GetMEs*.

778 **Differential module expression analysis**

779 To test for differences in module gene expression by genotype, we analyzed each module identified in
780 glutamatergic neurons by plotting the log fold change (logFC) of its member genes based on pseudo-
781 bulk differential expression analysis. We then compared the median logFC of each module to that of
782 the corresponding 'grey' module using a t-test, applying Bonferroni correction for multiple comparisons.
783 Modules with a Bonferroni-adjusted p-value < 0.05 in at least one glutamatergic subtype were
784 considered significantly differentially expressed.

785 **GO enrichment analysis**

786 GO analysis was performed on significant DEGs and DEMs using *enrichGO,* with the gene universe
787 being set to all genes expressed in the cell type the DEGs or DEMs were identified in. Genes and
788 modules were annotated with biological process and molecular function terms. Terms were deemed
789 significant if they had a corrected p-value < 0.05.
790

791 **Gene set enrichment analysis (GSEA)**

792 Gene set enrichment analysis was performed on DEGs from bulk and pseudobulk DE analysis using
793 the clusterProfiler R package[60] (version 4.10.0) with the org.Mm.eg.db database (version 3.18.0,
794 Carlson M (2022). _org.Mm.eg.db: Genome wide annotation for Mouse_. R package version 3.15.0.).
795 For pseudobulk DEGs, gene hits from each cell type were filtered to include only genes with adjusted p-
796 value < 0.05 and absolute LogFC > 0.25. Enrichment testing was conducted separately for upregulated
797 and downregulated gene sets using the enrichGO() function, with background genes defined as all
798 genes tested for differential expression in the corresponding analysis. Multiple testing correction was
799 applied using the Benjamini-Hochberg method, and GO terms with adjusted p-values < 0.05 were
800 considered significant.
801

802 **Calcium Imaging - Stereotactic injections**

803 We utilized adult mice of either sex housed and bred in the UCSF animal facility. To image prefrontal
804 activity in acute slices from wildtype or mutant animals, mice were injected with
805 AAV5.hSyn.GCaMP6f.WPRE.SV40 (Penn Viral Core). Mice were anesthetized with 2% isoflurane and
806 mounted in a stereotactic frame. Craniotomies were made according to stereotaxic coordinates relative
807 to Bregma. Coordinates for injection into mPFC were (in mm relative to Bregma): +1.7 anterior–
808 posterior (AP), –0.3 mediolateral (ML) and –2.75 dorsoventral (DV). Imaging was performed 4-6 weeks
809 later.
810

811 **Slice preparation and imaging**

812 300 μm coronal slices were prepared as previously described[93]. Immediately after preparation slices
813 were transferred to an N-Methyl-D-Glucamine (NMDG)-based recovery solution for 10 minutes before
814 being transferred to ACSF for the remainder of their recovery. The NMDG-based solution was
815 maintained at 32° C, and consisted of the following (in mM): 93 N-Methyl-D-Glucamine (NMDG), 93
816 HCl, 2.5 KCl, 1.2 NaH2PO4, 30 NaHCO3, 25 glucose, 20 HEPES, 5 Na-ascorbate, 5 Na-pyruvate, 2
817 thiourea, 10 magnesium sulfate, 0.5 calcium chloride. ACSF contained the following (in mM): 126 NaCl,
818 26 NaHCO3, 2.5 KCl, 1.25 NaH2PO4, 1 MgCl2, 2 CaCl, and 10 glucose. For imaging slices were
819 perfused with 'Active' ACSF which was identical to normal ACSF except containing elevated KCl (3.5
820 mM vs 2 mM) and reduced CaCl (1.2 mM vs 2 mM). Slice data was acquired at 10 Hz on an Olympus
821 BX51 upright microscope with a 20× 1.0NA water immersion lens, 0.5× reducer (Olympus), and ORCA-
822 ER CCD Camera (Hamamatsu Photonics). Illumination was delivered using a Lambda DG4 arc lamp
823 (Sutter Instruments). Light was delivered through a 472/30 excitation filter, 495nm single band dichroic,
824 and 496nm long pass emission filter (Semrock). All movies consisted of 36000 frames acquired at 10Hz
825 (1 hr) with 4×4 sensor binning yielding a final resolution of 256 × 312 pixels. Light power during imaging
826 was 100 – 500 μW/mm2. The Micro Manager software suite (v1.4, NIH) was used to control all camera
827 parameters and acquire movies. When necessary, drift correction was conducted in MATLAB using
828 custom written code[94] modified to utilize individual neurons as fiducials, whose positions were averaged
829 and aligned every 5 seconds. We segmented neuronal signals using a modified PCA/ICA approach[95]
830 modified as previously described[96] so that each segment was expressed as a binary ROI consisting of
831 pixels representing a single neuron. To deconvolve neuronal signals from background neuropil signals,
832 we subtracted the mean signal from each identified segment from the mean value in pixels surrounding
833 the edge of the segment (we excluded pixels that belonged to another ROI). Signals were subsequently
834 lowpass filtered to remove high frequency noise using the Matlab command: designfilt('lowpassfir',
835 'PassbandFrequency', 0.5, 'StopbandFrequency', .65, 'PassbandRipple', 1, 'StopbandAttenuation', 25).
836 We then detected events corresponding to epochs in which each neuron was active using threshold-
837 based event detection as previously described4. We detected increases in (F-F0)/F0 exceeding 2.5σ
838 over one frame, and then further thresholded these events by keeping only those events which

839 exceeded a 8σ increase over baseline and had an integrated area of 200 σ. σ is the standard deviation
840 of (F-F0)/F0. All further analysis was performed on binary rasters of detected events for each slice.
841

842 **Cranial Window Implantation Surgery**

843 Cranial window implantation in adult mice (6–8 weeks old) was performed as previously described[97].
844 Briefly, the mouse was anaesthetized by gaseous isoflurane (4% for induction, 1.5-2% for
845 maintenance) delivered through a vaporizer system and mounted on a stereotaxic frame. Throughout
846 the surgery the mouse was kept warm with a heating pad. Ophthalmic ointment was applied to prevent
847 eye desiccation and irritation. Carprofen (5 mg/kg, i.p.), buprenorphine (0.1 mg/kg, s.c.), enrofloxacin (5
848 mg/kg, s.c.), and dexamethasone (2 mg/kg, intramuscular) were administered. The fur over the surgical
849 site was shaved, and the scalp was cleaned with 3 rounds of alternating 70% ethanol and iodine
850 solution (Betadine®). A midline scalp incision was made, and the periosteum was gently scraped off
851 from the skull using a scalpel. A circular piece of the skull (centered at AP = –1 mm, ML = 1.5 mm) was
852 removed with a trephine (diameter = 2.3 mm, Fine Science Tools, Foster City, CA, USA) driven by a
853 high-speed micro-drill (Foredom K1070, Blackstone Industries, LLC, Bethal, CT, USA). The imaging
854 port was made by gluing a circular cover glass (#2, diameter = 2.2 mm) underneath a donut-shaped
855 glass (#1, inner diameter = 2 mm, outer diameter = 3 mm; Potomac Photonics, Inc., Baltimore, MD,
856 USA). The imaging port was mounted so that the bottom cover glass fit snugly into the cranial window
857 and the top glass donut rested above the skull. The imaging port was secured with a UV-cured
858 adhesive (Fusion Flo, Prevest DenPro, Jammu, India) onto the skull. After the solidification of the
859 adhesive, the scalp flaps were closed with suture. After 2 weeks of recovery, the central piece of the
860 scalp was excised, the edge of the scalp flap was secured to the tissue underneath with cyanoacrylate
861 (Vetbond), and a custom-made stainless-steel head-bar was secured over the skull with dental cement
862 (Jet Denture Repair, Lang Dental, Wheeling, IL, USA). The mouse received enrofloxacin,
863 buprenorphine, and carprofen once per day for two extra days post-surgery and was allowed to recover
864 for an additional week prior to imaging.
865

866 **Thin skull preparation**

867 The thin skull procedure was performed on adolescent (1 month old) mice as previously described[98].
868 Briefly, the mouse was anesthetized with a mixture of ketamine (20 mg/ml) and xylazine (2.0 mg/ml) in
869 0.9% sterile saline administered intraperitoneally (5 ml/kg body weight). Ophthalmic ointment was
870 applied to the eyes to prevent desiccation and irritation, and the fur over the scalp was removed with a
871 blade. A midline incision was made through the scalp and the periosteum was gently scraped off from
872 the skull. A high-speed micro-drill (Foredom K1070, Blackstone Industries, LLC, Bethal, CT, USA) and
873 a microblade were used to thin a small region of the skull to ~20 μm thickness. A custom-made head-
874 plate with a central opening was attached to the skull by cyanoacrylate glue (Krazy Glue, Elmer's
875 Products, Westerville, OH, USA), centered over the thinned region. The head-plate was secured onto a
876 custom-made metal baseplate to stabilize the mouse's head during imaging. Two-photon imaging was
877 performed as described above. After imaging, the head-plate was detached from the skull, the skull
878 was cleaned with sterile saline, and the scalp was sutured. The same region was imaged again 7 days
879 later.

880

881 **In vivo two-photon (2P) imaging and analysis**

882 2P imaging of dendritic spines was performed on a 2P microscope (Ultima IV, Bruker Co., Middleton,
883 WI) equipped with a 40× NA = 0.8 water immersion objective (LUMPlanFl/IR, Olympus, Japan) and an
884 ultrafast 2P laser (Mai Tai, Spectra-Physics, Santa Clara, CA) operating at 940 nm. The mouse was
885 anaesthetized with an intraperitoneal injection of a mixture of 85 mg/kg ketamine and 8.5 mg/kg
886 xylazine in 0.9% saline and mounted on a custom-made stage for imaging. Stacks of images were
887 acquired with a Z-step size of 1 μm at 4X zoom. Relocation of the same dendrites in subsequent
888 imaging sessions was achieved by reference to blood vessels and the dendritic branching pattern. The
889 same dendrites were imaged again 1 week after the first imaging session.

890 Data analysis was performed in ImageJ as previously described[98]. Typically, 150–200 spines were
891 analyzed per animal per session. The percentage of spines formed/eliminated was calculated as the
892 number of spines formed/eliminated divided by the total number of spines counted from the previous

893 imaging session. Dendritic spine density was calculated as the number of dendritic spines per 10 μm of
894 dendritic segment length on the first imaging day.
895
896 **EEG/EMG recording and analysis**
897 The EEG/EMG implant consists of a mini connector (Samtec Inc., SFMC-102-01-S-D) soldered to 2
898 EEG and 2 EMG electrodes made from Teflon-coated, multi-filament stainless steel wires (0.002" in
899 diameter, Medwire 316 SS7/44T, Sigmund Cohn Corp.). The mouse was anaesthetized by gaseous
900 isoflurane (4% for induction, 1.5-2% for maintenance) delivered through a vaporizer system and
901 mounted on a stereotaxic frame. Throughout the surgery the mouse was kept warm with a heating pad.
902 Ophthalmic ointment was applied to prevent eye desiccation and irritation. Buprenorphine (0.1 mg/kg,
903 s.c.), carprofen (5 mg/kg, i.p.), and enrofloxacin (5 mg/kg, s.c.) were injected. The fur over the surgical
904 site was shaved, and the scalp was cleaned with 3 rounds of alternating 70% ethanol and iodine
905 solution (Betadine®). A piece of the scalp was excised with scissors to expose the skull. The edge of
906 the scalp flap was secured to the tissue underneath with cyanoacrylate (Vetbond). The exposed skull
907 surface was gently scraped with a scalpel to remove the periosteum. Small holes (one at AP = + 2 mm,
908 ML = 2 mm; the other at AP = -3 mm, ML = 2 mm) were drilled through the skull using a high speed
909 microdrill (Foredom K.1070) with fine drill bits. The EEG electrodes were inserted into the holes,
910 positioned between the skull and the brain surface, and secured with a UV-curable adhesive (Fusion
911 Flo, Prevest DenPro). The EMG electrodes were positioned under the nuchal trapezoid muscles and
912 secured with Vetbond. The exposed skull surface was covered with a thin layer of Vetbond. The
913 EEG/EMG implant connector was then further secured onto the skull by dental cement (Jet Denture
914 Repair, Lang Dental). Enrofloxacin (5 mg/kg, s.c.) and carprofen (5 mg/kg, i.p.) were given at 24 h after
915 surgery. The mouse was allowed to recover for 7 days before EEG/EMG recording starts. A BL-420N
916 biological signal acquisition and processing system (Chengdu Techman, China) was used for
917 EEG/EMG recording. EEG was sampled at 200 Hz and band-pass filtered between 1-100 Hz; EMG
918 was sampled at 200 Hz and band-pass filtered between 1-2K Hz. Recorded data was annotated

manually and subsequently processed using custom-written Matlab programs (R2022, MathWorks Inc.).

922 **REFERENCES**

923

924 1. Fu, J. M. *et al.* Rare coding variation provides insight into the genetic architecture and
925 phenotypic context of autism. *Nat. Genet.* **54**, 1320–1331 (2022).
926 2. Satterstrom, F. K. *et al.* Large-Scale Exome Sequencing Study Implicates Both Developmental
927 and Functional Changes in the Neurobiology of Autism. *Cell* **180**, 568-584.e23 (2020).
928 3. Alotaibi, M. & Ramzan, K. A de novo variant of CHD8 in a patient with autism spectrum
929 disorder. *Discov. Craiova Rom.* **8**, e107 (2020).
930 4. An, Y. *et al.* De novo variants in the Helicase-C domain of CHD8 are associated with severe
931 phenotypes including autism, language disability and overgrowth. *Hum. Genet.* **139**, 499–512
932 (2020).
933 5. Beighley, J. S. *et al.* Clinical Phenotypes of Carriers of Mutations in CHD8 or Its Conserved
934 Target Genes. *Biol. Psychiatry* **87**, 123–131 (2020).
935 6. Bernier, R. *et al.* Disruptive CHD8 Mutations Define a Subtype of Autism Early in Development.
936 *Cell* **158**, 263–276 (2014).
937 7. Doummar, D. *et al.* Childhood-onset progressive dystonia associated with pathogenic
938 truncating variants in CHD8. *Ann. Clin. Transl. Neurol.* **8**, 1986–1990 (2021).
939 8. Douzgou, S. *et al.* The clinical presentation caused by truncating CHD8 variants. *Clin. Genet.*
940 **96**, 72–84 (2019).
941 9. Ostrowski, P. J. *et al.* The CHD8 overgrowth syndrome: A detailed evaluation of an emerging
942 overgrowth phenotype in 27 patients. *Am. J. Med. Genet. C Semin. Med. Genet.* **181**, 557–564
943 (2019).
944 10. Amaral, D. G. *et al.* In pursuit of neurophenotypes: The consequences of having autism and a
945 big brain. *Autism Res. Off. J. Int. Soc. Autism Res.* **10**, 711–722 (2017).

946 11. Barnard, R. A., Pomaville, M. B. & O'Roak, B. J. Mutations and Modeling of the Chromatin
947 Remodeler CHD8 Define an Emerging Autism Etiology. *Front. Neurosci.* **9**, (2015).
948 12. Cotney, J. *et al.* The autism-associated chromatin modifier CHD8 regulates other autism risk
949 genes during human neurodevelopment. *Nat. Commun.* **6**, 6404 (2015).
950 13. Willsey, H. R., Willsey, A. J., Wang, B. & State, M. W. Genomics, convergent neuroscience and
951 progress in understanding autism spectrum disorder. *Nat. Rev. Neurosci.* **23**, 323–341 (2022).
952 14. Levy, D. *et al.* Rare De Novo and Transmitted Copy-Number Variation in Autistic Spectrum
953 Disorders. *Neuron* **70**, 886–897 (2011).
954 15. O'Roak, B. J. *et al.* Sporadic autism exomes reveal a highly interconnected protein network of
955 de novo mutations. *Nature* **485**, 246–250 (2012).
956 16. O'Roak, B. J. *et al.* Exome sequencing in sporadic autism spectrum disorders identifies severe
957 de novo mutations. *Nat. Genet.* **43**, 585–589 (2011).
958 17. Ronemus, M., Iossifov, I., Levy, D. & Wigler, M. The role of de novo mutations in the genetics of
959 autism spectrum disorders. *Nat. Rev. Genet.* **15**, 133–141 (2014).
960 18. Yuen, R. K. *et al.* Genome-wide characteristics of de novo mutations in autism. *Npj Genomic*
961 *Med.* **1**, 1–10 (2016).
962 19. Nishiyama, M. *et al.* Early Embryonic Death in Mice Lacking the β-Catenin-Binding Protein
963 Duplin. *Mol. Cell. Biol.* **24**, 8386–8394 (2004).
964 20. Gompers, A. L. *et al.* Germline Chd8 haploinsufficiency alters brain development in mouse.
965 *Nat. Neurosci.* **20**, 1062–1073 (2017).
966 21. Jung, H. *et al.* Sexually dimorphic behavior, neuronal activity, and gene expression in Chd8-
967 mutant mice. *Nat. Neurosci.* **21**, 1218–1228 (2018).

968 22. Katayama, Y. *et al.* CHD8 haploinsufficiency results in autistic-like phenotypes in mice.
969 *Nature* **537**, 675–679 (2016).
970 23. Niu, X. *et al.* The Deficiency of the ASD-Related Gene CHD8 Disrupts Behavioral Patterns and
971 Inhibits Hippocampal Neurogenesis in Mice. *J. Mol. Neurosci. MN* **74**, 103 (2024).
972 24. Platt, R. J. *et al.* Chd8 Mutation Leads to Autistic-like Behaviors and Impaired Striatal Circuits.
973 *Cell Rep.* **19**, 335–350 (2017).
974 25. Suetterlin, P. *et al.* Altered Neocortical Gene Expression, Brain Overgrowth and Functional
975 Over-Connectivity in Chd8 Haploinsufficient Mice. *Cereb. Cortex N. Y. N 1991* **28**, 2192–2206
976 (2018).
977 26. Jiménez, J. A. *et al.* Chd8 haploinsufficiency impairs early brain development and protein
978 homeostasis later in life. *Mol. Autism* **11**, 74 (2020).
979 27. Jiménez, J. A. *et al.* Chd8 haploinsufficiency impairs early brain development and protein
980 homeostasis later in life. *Mol. Autism* **11**, 74 (2020).
981 28. Durak, O. *et al.* Chd8 mediates cortical neurogenesis via transcriptional regulation of cell
982 cycle and Wnt signaling. *Nat. Neurosci.* **19**, 1477–1488 (2016).
983 29. Yim, K. M. *et al.* Cell type-specific dysregulation of gene expression due to Chd8
984 haploinsufficiency during mouse cortical development. *bioRxiv* 2024.08.14.608000 (2024)
985 doi:10.1101/2024.08.14.608000.
986 30. Hurley, S. *et al.* Distinct, dosage-sensitive requirements for the autism-associated factor
987 CHD8 during cortical development. *Mol. Autism* **12**, 16 (2021).
988 31. Astorkia, M., Liu, Y., Pedrosa, E. M., Lachman, H. M. & Zheng, D. Molecular and network
989 disruptions in neurodevelopment uncovered by single cell transcriptomics analysis of CHD8

990 heterozygous cerebral organoids. Preprint at https://doi.org/10.1101/2023.09.27.559752
991 (2023).
992 32. Paulsen, B. *et al.* Autism genes converge on asynchronous development of shared neuron
993 classes. *Nature* **602**, 268–273 (2022).
994 33. Hoffmann, A. & Spengler, D. Single-Cell Transcriptomics Supports a Role of CHD8 in Autism.
995 *Int. J. Mol. Sci.* **22**, 3261 (2021).
996 34. Tabbaa, M., Knoll, A. & Levitt, P. Mouse population genetics phenocopies heterogeneity of
997 human Chd8 haploinsufficiency. *Neuron* **111**, 539-556.e5 (2023).
998 35. Tabbaa, M. & Levitt, P. Chd8 haploinsufficiency impacts rearing experience in C57BL/6 mice.
999 *Genes Brain Behav.* **23**, e12892 (2024).
000 36. Ellingford, R. A. *et al.* Cell-type-specific synaptic imbalance and disrupted homeostatic
001 plasticity in cortical circuits of ASD-associated Chd8 haploinsufficient mice. *Mol. Psychiatry*
002 **26**, 3614–3624 (2021).
003 37. Ellingford, R. A., Tojo, M., Basson, M. A. & Andreae, L. C. Male-Dominant Effects of Chd8
004 Haploinsufficiency on Synaptic Phenotypes during Development in Mouse Prefrontal Cortex.
005 *ACS Chem. Neurosci.* **15**, 1635–1642 (2024).
006 38. Villa, C. E. *et al.* CHD8 haploinsufficiency links autism to transient alterations in excitatory
007 and inhibitory trajectories. *Cell Rep.* **39**, 110615 (2022).
008 39. Li, B. *et al.* CHD8 mutations increase gliogenesis to enlarge brain size in the nonhuman
009 primate. *Cell Discov.* **9**, 27 (2023).
010 40. Shi, X. *et al.* Heterozygous deletion of the autism-associated gene CHD8 impairs synaptic
011 function through widespread changes in gene expression and chromatin compaction. *Am. J.*
012 *Hum. Genet.* **110**, 1750–1768 (2023).

013 41. Gao, Y. *et al.* Multimodal analyses reveal genes driving electrophysiological maturation of
014 neurons in the primate prefrontal cortex. Preprint at
015 https://doi.org/10.1101/2023.06.02.543460 (2024).
016 42. Kweon, H. *et al.* Excitatory neuronal CHD8 in the regulation of neocortical development and
017 sensory-motor behaviors. *Cell Rep.* **34**, 108780 (2021).
018 43. Haddad Derafshi, B. *et al.* The autism risk factor CHD8 is a chromatin activator in human
019 neurons and functionally dependent on the ERK-MAPK pathway effector ELK1. *Sci. Rep.* **12**,
020 22425 (2022).
021 44. Kawamura, A. & Nishiyama, M. Deletion of the autism-related gene Chd8 alters activity-
022 dependent transcriptional responses in mouse postmitotic neurons. *Commun. Biol.* **6**, 593
023 (2023).
024 45. Dong, C. *et al.* Conserved and Distinct Functions of the Autism-Related Chromatin Remodeler
025 CHD8 in Embryonic and Adult Forebrain Neurogenesis. *J. Neurosci. Off. J. Soc. Neurosci.* **42**,
026 8373–8392 (2022).
027 46. Chen, X. *et al.* Deletion of CHD8 in cerebellar granule neuron progenitors leads to severe
028 cerebellar hypoplasia, ataxia, and psychiatric behavior in mice. *J. Genet. Genomics Yi Chuan*
029 *Xue Bao* **49**, 859–869 (2022).
030 47. Kawamura, A. *et al.* Oligodendrocyte dysfunction due to Chd8 mutation gives rise to
031 behavioral deficits in mice. *Hum. Mol. Genet.* **29**, 1274–1291 (2020).
032 48. Kawamura, A. *et al.* Chd8 mutation in oligodendrocytes alters microstructure and functional
033 connectivity in the mouse brain. *Mol. Brain* **13**, 160 (2020).

034 49. Zhao, C. *et al.* Dual Requirement of CHD8 for Chromatin Landscape Establishment and
035 Histone Methyltransferase Recruitment to Promote CNS Myelination and Repair. *Dev. Cell* **45**,
036 753-768.e8 (2018).
037 50. Megagiannis, P. *et al.* Autism-associated CHD8 controls reactive gliosis and
038 neuroinflammation via remodeling chromatin in astrocytes. *Cell Rep.* **43**, 114637 (2024).
039 51. Takanezawa, Y. *et al.* Microglial ASD-related genes are involved in oligodendrocyte
040 differentiation. *Sci. Rep.* **11**, 17825 (2021).
041 52. Spear, L. P. The adolescent brain and age-related behavioral manifestations. *Neurosci.*
042 *Biobehav. Rev.* **24**, 417–463 (2000).
043 53. West, M. J. & Gundersen, H. J. Unbiased stereological estimation of the number of neurons in
044 the human hippocampus. *J. Comp. Neurol.* **296**, 1–22 (1990).
045 54. Lavenex, P. B. Lesions in the budgerigar vocal control nucleus NLc affect production, but not
046 memory, of english words and natural vocalizations. *J. Comp. Neurol.* **421**, 437–460 (2000).
047 55. West, M. J., Slomianka, L. & Gundersen, H. J. Unbiased stereological estimation of the total
048 number of neurons in thesubdivisions of the rat hippocampus using the optical fractionator.
049 *Anat. Rec.* **231**, 482–497 (1991).
050 56. Young, M. D. & Behjati, S. SoupX removes ambient RNA contamination from droplet-based
051 single-cell RNA sequencing data. *GigaScience* **9**, giaa151 (2020).
052 57. Yao, Z. *et al.* A high-resolution transcriptomic and spatial atlas of cell types in the whole
053 mouse brain. *BioRxiv Prepr. Serv. Biol.* 2023.03.06.531121 (2023)
054 doi:10.1101/2023.03.06.531121.
055 58. Murphy, A. E. & Skene, N. G. A balanced measure shows superior performance of pseudobulk
056 methods in single-cell RNA-sequencing analysis. *Nat. Commun.* **13**, 7851 (2022).

057 59. Love, M. I., Huber, W. & Anders, S. Moderated estimation of fold change and dispersion for
058 RNA-seq data with DESeq2. *Genome Biol.* **15**, 1–21 (2014).
059 60. Wu, T. *et al.* clusterProfiler 4.0: A universal enrichment tool for interpreting omics data. *Innov.*
060 *Camb. Mass* **2**, 100141 (2021).
061 61. Zhao, W., Johnston, K. G., Ren, H., Xu, X. & Nie, Q. Inferring neuron-neuron communications
062 from single-cell transcriptomics through NeuronChat. *Nat. Commun.* **14**, 1128 (2023).
063 62. Morabito, S., Reese, F., Rahimzadeh, N., Miyoshi, E. & Swarup, V. hdWGCNA identifies co-
064 expression networks in high-dimensional transcriptomics data. *Cell Rep. Methods* **3**, 100498
065 (2023).
066 63. Yoo, T. *et al.* A DLG2 deficiency in mice leads to reduced sociability and increased repetitive
067 behavior accompanied by aberrant synaptic transmission in the dorsal striatum. *Mol. Autism*
068 **11**, 19 (2020).
069 64. Yoo, T. *et al.* A Deficiency of the Psychiatric Risk Gene DLG2/PSD-93 Causes Excitatory
070 Synaptic Deficits in the Dorsolateral Striatum. *Front. Mol. Neurosci.* **15**, 938590 (2022).
071 65. Sanders, B. *et al.* Transcriptional programs regulating neuronal differentiation are disrupted in
072 DLG2 knockout human embryonic stem cells and enriched for schizophrenia and related
073 disorders risk variants. *Nat. Commun.* **13**, 27 (2022).
074 66. Chang, X. *et al.* Common and Rare Genetic Risk Factors Converge in Protein Interaction
075 Networks Underlying Schizophrenia. *Front. Genet.* **9**, 434 (2018).
076 67. Feng, G. *et al.* Imaging neuronal subsets in transgenic mice expressing multiple spectral
077 variants of GFP. *Neuron* **28**, 41–51 (2000).

078 68. Wang, P. *et al.* CRISPR/Cas9-mediated heterozygous knockout of the autism gene CHD8 and
079 characterization of its transcriptional networks in neurodevelopment. *Mol. Autism* **6**, 55
080 (2015).
081 69. Haddad Derafshi, B. *et al.* The autism risk factor CHD8 is a chromatin activator in human
082 neurons and functionally dependent on the ERK-MAPK pathway effector ELK1. *Sci. Rep.* **12**,
083 22425 (2022).
084 70. Earl, R. K. *et al.* Sleep Problems in Children with ASD and Gene Disrupting Mutations. *J. Genet.*
085 *Psychol.* **182**, 317–334 (2021).
086 71. topGO. *Bioconductor* http://bioconductor.org/packages/topGO/.
087 72. Kerschbamer, E. *et al.* CHD8 suppression impacts on histone H3 lysine 36 trimethylation and
088 alters RNA alternative splicing. *Nucleic Acids Res.* **50**, 12809–12828 (2022).
089 73. Wade, A. A., Lim, K., Catta-Preta, R. & Nord, A. S. Common CHD8 Genomic Targets Contrast
090 With Model-Specific Transcriptional Impacts of CHD8 Haploinsufficiency. *Front. Mol.*
091 *Neurosci.* **11**, 481 (2018).
092 74. Zaghlool, A. *et al.* Characterization of the nuclear and cytosolic transcriptomes in human
093 brain tissue reveals new insights into the subcellular distribution of RNA transcripts. *Sci. Rep.*
094 **11**, 4076 (2021).
095 75. Bakken, T. E. *et al.* Single-nucleus and single-cell transcriptomes compared in matched
096 cortical cell types. *PloS One* **13**, e0209648 (2018).
097 76. Squair, J. W. *et al.* Confronting false discoveries in single-cell differential expression. *Nat.*
098 *Commun.* **12**, 5692 (2021).
099 77. Chareyron, L. J., Banta Lavenex, P., Amaral, D. G. & Lavenex, P. Stereological analysis of the
100 rat and monkey amygdala. *J. Comp. Neurol.* **519**, 3218–3239 (2011).

78. Lavenex, P., Lavenex, P. B., Bennett, J. L. & Amaral, D. G. Postmortem changes in the neuroanatomical characteristics of the primate brain: hippocampal formation. *J. Comp. Neurol.* **512**, 27–51 (2009).

79. *Paxinos and Franklin's the Mouse Brain in Stereotaxic Coordinates*. (2019).

80. Gundersen, H. J. & Jensen, E. B. The efficiency of systematic sampling in stereology and its prediction. *J. Microsc.* **147**, 229–263 (1987).

81. Gundersen, H. J. Stereology of arbitrary particles. A review of unbiased number and size estimators and the presentation of some new ones, in memory of William R. Thompson. *J. Microsc.* **143**, 3–45 (1986).

82. Long, J. M. *et al.* Stereological estimation of total microglia number in mouse hippocampus. *J. Neurosci. Methods* **84**, 101–108 (1998).

83. García-Cabezas, M. Á., John, Y. J., Barbas, H. & Zikopoulos, B. Distinction of Neurons, Glia and Endothelial Cells in the Cerebral Cortex: An Algorithm Based on Cytological Features. *Front. Neuroanat.* **10**, 107 (2016).

84. Haida, O. *et al.* Sex-dependent behavioral deficits and neuropathology in a maternal immune activation model of autism. *Transl. Psychiatry* **9**, 124 (2019).

85. Lauber, E., Filice, F. & Schwaller, B. Dysregulation of Parvalbumin Expression in the Cntnap2-/- Mouse Model of Autism Spectrum Disorder. *Front. Mol. Neurosci.* **11**, 262 (2018).

86. Gundersen, H. J. The nucleator. *J. Microsc.* **151**, 3–21 (1988).

87. Wickham, H. *Ggplot2: Elegant Graphics for Data Analysis*. (Springer, New York, NY, 2009). doi:10.1007/978-0-387-98141-3.

88. Dobin, A. *et al.* STAR: ultrafast universal RNA-seq aligner. *Bioinforma. Oxf. Engl.* **29**, 15–21 (2013).

124 89. Liao, Y., Smyth, G. K. & Shi, W. featureCounts: an efficient general purpose program for
125 assigning sequence reads to genomic features. *Bioinforma. Oxf. Engl.* **30**, 923–930 (2014).
126 90. Babraham Bioinformatics - FastQC A Quality Control tool for High Throughput Sequence Data.
127 https://www.bioinformatics.babraham.ac.uk/projects/fastqc/.
128 91. Robinson, M. D., McCarthy, D. J. & Smyth, G. K. edgeR: a Bioconductor package for differential
129 expression analysis of digital gene expression data. *Bioinforma. Oxf. Engl.* **26**, 139–140 (2010).
130 92. Leek, J. T., Johnson, W. E., Parker, H. S., Jaffe, A. E. & Storey, J. D. The sva package for
131 removing batch effects and other unwanted variation in high-throughput experiments.
132 *Bioinforma. Oxf. Engl.* **28**, 882–883 (2012).
133 93. Luongo, F. J., Horn, M. E. & Sohal, V. S. Putative Microcircuit-Level Substrates for Attention Are
134 Disrupted in Mouse Models of Autism. *Biol. Psychiatry* **79**, 667–675 (2016).
135 94. Frost, N. A., Shroff, H., Kong, H., Betzig, E. & Blanpied, T. A. Single-molecule discrimination of
136 discrete perisynaptic and distributed sites of actin filament assembly within dendritic spines.
137 *Neuron* **67**, 86–99 (2010).
138 95. Mukamel, E. A., Nimmerjahn, A. & Schnitzer, M. J. Automated analysis of cellular signals from
139 large-scale calcium imaging data. *Neuron* **63**, 747–760 (2009).
140 96. Frost, N. A., Haggart, A. & Sohal, V. S. Dynamic patterns of correlated activity in the prefrontal
141 cortex encode information about social behavior. *PLoS Biol.* **19**, e3001235 (2021).
142 97. Lu, J. *et al.* An analog of psychedelics restores functional neural circuits disrupted by
143 unpredictable stress. *Mol. Psychiatry* **26**, 6237–6252 (2021).
144 98. Xu, T. *et al.* Rapid formation and selective stabilization of synapses for enduring motor
145 memories. *Nature* **462**, 915–919 (2009).
146